



# Available online at www.sciencedirect.com

# **ScienceDirect**

Comput. Methods Appl. Mech. Engrg. 365 (2020) 112985

Computer methods in applied mechanics and engineering

www.elsevier.com/locate/cma

# The treatment of the Neumann boundary conditions for a new numerical approach to the solution of PDEs with optimal accuracy on irregular domains and Cartesian meshes

A. Idesman\*, B. Dey

Department of Mechanical Engineering, Texas Tech University, Lubbock, TX 79409-1021, USA
Received 27 July 2019; received in revised form 6 February 2020; accepted 5 March 2020
Available online xxxx

#### Abstract

Recently we have developed a new 3-D numerical approach for the time dependent wave and heat equations as well as for the time independent Poisson equation on irregular domains with the Dirichlet boundary conditions. Its extension to the Neumann boundary conditions that was a big issue due to the presence of normal derivatives along irregular boundaries is considered in this paper. Trivial Cartesian meshes and simple 27-point uniform and nonuniform stencil equations are used with the new approach for 3-D irregular domains. The Neumann boundary conditions are introduced as the known right-hand side into the stencil and do not change the width of the stencil. The calculation of the coefficients of the stencil equations is based on the minimization of the local truncation error of the stencil equations and yields the optimal order of accuracy of the new technique. Very small distances  $(0.1 \ h-10^{-9} \ h$  where h is the grid size) between the grid points of a Cartesian mesh and the boundary do not worsen the accuracy of the new technique. At similar 27-point stencils, the accuracy of the new approach is much higher than that for the linear finite elements. The numerical results for irregular domains show that at the same number of degrees of freedom, the new approach is even much more accurate than the high-order (up to the fourth order) tetrahedral finite elements with much wider stencils. The wave and heat equations can be uniformly treated with the new approach. The order of the time derivative in these equations does not affect the coefficients of the stencil equations of the semi-discrete systems. The new approach can be directly applied to other partial differential equations.

© 2020 Elsevier B.V. All rights reserved.

Keywords: Neumann boundary conditions; Local truncation error; Irregular domains; Cartesian meshes; Optimal accuracy; Wave, heat and Poisson equations

## 1. Introduction

The finite element method, the finite volume method, the isogeometric elements, the spectral elements and similar techniques represent very powerful tools for the solution of partial differential equations (PDEs) for a complex geometry. However, the generation of non-uniform meshes for a complex 3-D geometry is not simple and may lead to the decrease in accuracy of these techniques if 'bad' elements (e.g., elements with small angles) appear in the mesh. Moreover, the conventional derivation of discrete equations for these techniques (e.g., based on the Galerkin

E-mail address: alexander.idesman@ttu.edu (A. Idesman).

<sup>\*</sup> Corresponding author.

approaches) does not lead to the optimal accuracy. For example, it has been shown in many publications on wave propagation that at the same width of the stencil equations of a semi-discrete system for regular rectangular domains with uniform meshes, the accuracy of the conventional linear finite elements can be improved from order two to order four (e.g., see [1–8] and others), the accuracy of the conventional high-order finite and isogeometric elements can be improved from order 2p to order 2p+2 (e.g., see [9-13]) where p is the element order. These improvements are based on the use of the averaged mass matrix or on the use of the special locations of the integration points for the calculation of the elemental mass and stiffness matrices. However, the increase in the order of accuracy for the high-order elements in [9–13] is not optimal. In [14–16] the order of accuracy of the high-order elements on rectangular domains has been improved to 4p and this order is optimal at a given width of stencil equations. There is a significant number of publications related to the numerical solution of different PDEs on irregular domains with uniform embedded meshes. For example, we can mention the following fictitious domain numerical methods that use uniform embedded meshes: the embedded finite difference method, the cut finite element method, the finite cell method, the Cartesian grid method, the immersed interface method, the virtual boundary method, the embedded boundary method, etc. The main objective of these techniques is to simplify the mesh generation for irregular domains as well as to mitigate the effect of 'bad' elements. For example, the techniques based on the finite element formulations (such as the cut finite element method, the finite cell method, the virtual boundary method and others) yield the p+1 order of accuracy even with small cut cells generated due to complex irregular boundaries (e.g., see [17–23] and many others). The main advantage of the embedded boundary method developed in [24–28] is the use of a simple Cartesian mesh. The boundary conditions or fluxes in this technique are interpolated using the Cartesian grid points and this leads to the increase in the stencil width for the grid points located close to the boundary (the numerical techniques developed in [24–28] provide just the second order of accuracy for the global solution). Therefore, the development of robust numerical techniques for the solution of PDEs on irregular domains that provide an optimal and high order of accuracy is still a challenging problem.

Recently in our papers [29–31] we have developed a new numerical technique for the solution of PDEs that yields an optimal accuracy for a given structure of discrete or semidiscrete equations. Currently it is implemented for the wave, heat and Poisson equations. We called this approach the optimal local truncation error method (OLTEM); see [29,30]. The main features and advantages of the new approach are a high optimal accuracy as well as the use of trivial Cartesian meshes that are modified in a simple manner in the vicinity of boundaries of complex irregular domains. In contrast to the finite element, finite volume, isogeometric element and similar techniques, there is no need in complicated mesh generators for multidimensional problems with irregular domains with the proposed technique. At the same structure of the semidiscrete or discrete equations, the new technique provides the optimal order of accuracy that exceeds the order of accuracy of many known numerical approaches on regular and irregular domains. In [29-31] we showed that the new approach can be easily implemented in the 2-D and 3-D cases for the Dirichlet boundary conditions. The structure of the stencil equations for the new approach with the Dirichlet boundary conditions is similar to that for the linear quadrilateral finite elements on Cartesian meshes. We were not able to develop the new approach with the Neumann boundary conditions using the stencils similar to those for the linear quadrilateral finite elements. However, we implemented the new approach with the Neumann boundary conditions in [29,30] for the 2-D case using a special selection of the grid points included into the stencils. This selection depends on the location of a Cartesian grid with respect to the boundary with the Neumann boundary conditions. The extension of this 2-D approach to 3-D irregular domains with the Neumann boundary conditions becomes intractable (at least, we were not able to implement it in the 3-D case). We should also mention that the different stencil equations were used in [29,30] for the Dirichlet and Neumann boundary conditions.

In this paper we will show that the Neumann boundary conditions can be also implemented with the compact stencil equations that are similar to those for the Dirichlet boundary conditions. These new findings allow us to solve not only 2-D problems but also 3-D problems with the Neumann boundary conditions for any complex irregular domains. Similar to our previous papers, here we apply the new numerical approach to the time-dependent wave and heat equations as well as to the time-independent Poisson equation on 3-D irregular domains with the Neumann and Dirichlet boundary conditions.

Wave propagation in an isotropic homogeneous medium is described by the following scalar wave equation in domain  $\Omega$ :

$$\frac{\partial^2 u}{\partial t^2} - c^2 \nabla^2 u = f. \tag{1}$$

Similarly, the heat equation in domain  $\Omega$  can be written as:

$$\frac{\partial u}{\partial t} - a\nabla^2 u = f. \tag{2}$$

The Poisson equation in domain  $\Omega$  has the following form:

$$\nabla^2 u = f. ag{3}$$

In Eqs. (1)–(3), c is the wave velocity, a is the thermal diffusivity,  $f(\mathbf{x},t)$  is the loading (source) term, u is the field variable. The Neumann boundary conditions  $n_1 \frac{\partial u}{\partial x} + n_2 \frac{\partial u}{\partial y} + n_3 \frac{\partial u}{\partial z} = g_1$  are applied along the boundary  $\Gamma^s$ , the Dirichlet boundary conditions  $u = g_2$  are applied along the boundary  $\Gamma^u$  where the entire boundary  $\Gamma$  is  $\Gamma = \Gamma^s U \Gamma^u$  and  $n_i$  (i = 1, 2, 3) are the x-, y- and z-components of the outward unit normal vector. The initial conditions are  $u(\mathbf{x}, t = 0) = g_3$ ,  $v(\mathbf{x}, t = 0) = g_4$  in  $\Omega$  for the wave equation and  $u(\mathbf{x}, t = 0) = g_3$  in  $\Omega$  for the heat equation where  $g_i$  (i = 1, 2, 3, 4) are the given functions. According to the new approach, the semidiscrete system for the wave and heat equations after the space discretization with a Cartesian rectangular mesh can be represented as a system of ordinary differential equations in time. The ordinary differential equation of this system formed for each internal grid point is called the stencil equation and can be written down as follows:

$$\sum_{i=1}^{M} [h^2 m_i \frac{d^n u_i^{num}}{dt^n} + k_i u_i^{num}] = \tilde{f},$$
(4)

where  $u_i^{num}$  and  $\frac{d^n u_i^{num}}{dt^n}$  are the numerical solution for function u and its time derivative at the grid points,  $m_i$  and  $k_i$  are the unknown coefficients to be determined,  $\tilde{f}(t)$  is the discretized loading (source) term (see the next Sections), M is the number of the grid points included into the stencil equation, n=2 for the wave equation and n=1 for the heat equation, h is the mesh size along the x-axis. The stencil equation for the Poisson equation after the space discretization can be written as an algebraic equation:

$$\sum_{i=1}^{M} k_i u_i^{num} = \tilde{f}. \tag{5}$$

Many numerical techniques such as the finite difference method, the finite element method, the finite volume method, the isogeometric elements, the spectral elements, different meshless methods and others can be finally reduced to Eqs. (4) and (5) with some specific coefficients  $m_i$  and  $k_i$  for the wave, heat and Poisson equations. In the derivations below, we will assume 27-point stencils (N = 27) in the 3-D case that are similar to the 27-point stencils of the linear quadrilateral finite elements on Cartesian meshes. Generally, stencils with any number of grid points M can be used with the suggested approach.

Let us introduce the local truncation error used with the new approach. The replacement of the numerical values of the function  $u_i^{num}$  and its time derivatives  $\frac{d^n u_i^{num}}{dt^n}$  at the grid points in Eq. (4) by the exact solution  $u_i$  and  $\frac{d^n u_i}{dt^n}$  to the wave or heat equation, Eq. (1) or (2), leads to the residual e of this equation called the local truncation error of the semidiscrete equation, Eq. (4):

$$e = \sum_{i=1}^{M} [h^2 m_i \frac{d^n u_i}{dt^n} + k_i u_i] - \tilde{f}.$$
 (6)

Calculating the difference between Eqs. (6) and (4) we can get

$$e = \sum_{i=1}^{M} \{h^2 m_i \left[ \frac{d^n u_i}{dt^n} - \frac{d^n u_i^{num}}{dt^n} \right] + k_i \left[ u_i - u_i^{num} \right] \} = \sum_{i=1}^{M} [h^2 m_i \bar{e}_i^v + k_i \bar{e}_i^u],$$
 (7)

where  $\bar{e}_i^u = u_i - u_i^{num}$  and  $\bar{e}_i^v = \frac{d^n u_i}{dt^n} - \frac{d^n u_i^{num}}{dt^n}$  are the errors of the function u and its time derivatives at the grid points i. As can be seen from Eq. (7), the local truncation error e is a linear combination of the errors of the function u and its time derivatives at the grid points i which are included into the stencil equation. The local truncation error e for Eq. (5) can be obtained from Eqs. (6)–(7) with  $m_i = 0$ .

In Section 2 a new numerical approach with 27 point uniform and nonuniform stencils is uniformly derived for the 3-D wave and heat equations with zero and non-zero loading (source) term. In Section 3 we show that along

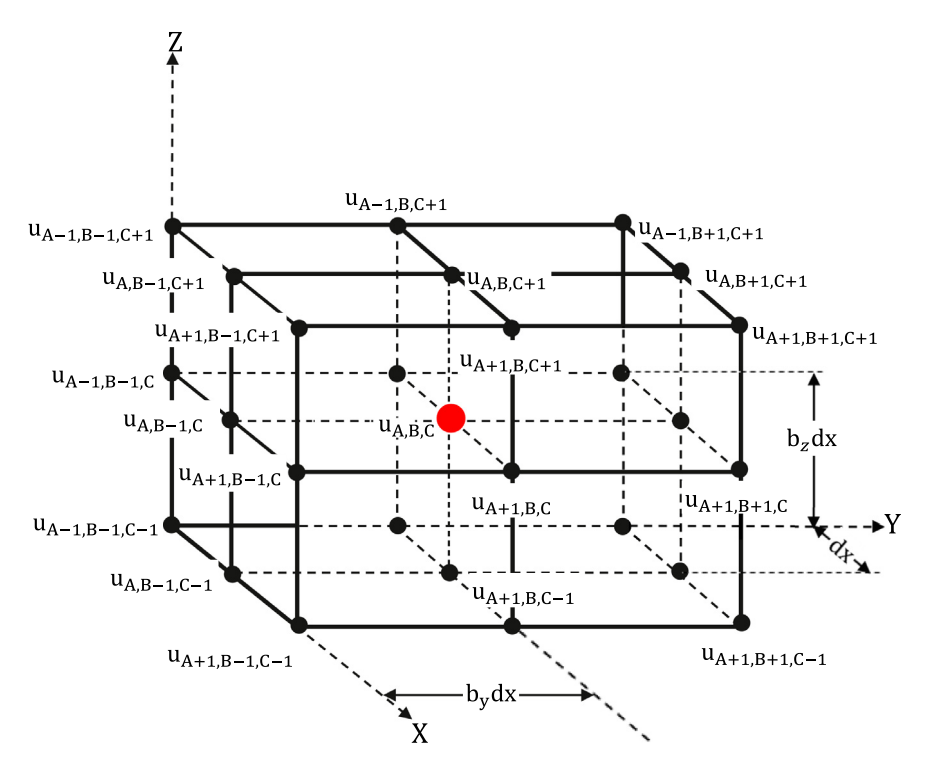


Fig. 1. The spatial locations of the degrees of freedom  $u_{i,j,k}$  (i = A - 1, A, A + 1, j = B - 1, B, B + 1 and k = C - 1, C, C + 1) contributing to the 27-point uniform stencil for the internal degree of freedom  $u_{A,B,C}$  located far from the boundary.

with the time dependent wave and heat equations, the new approach with 27 point uniform and nonuniform stencils can be similarly developed for the 3-D time independent Poisson equation with zero and non-zero loading (source) term. 3-D numerical examples with regular and irregular domains as well as the comparison with FEM are presented in Section 4. For the derivation of many analytical expressions presented below we use the computational program "Mathematica".

#### 2. A new numerical approach for the 3-D wave and heat equations

# 2.1. Zero load (source) f = 0 in Eqs. (1) and (2)

Here, we present 27-point uniform stencils that will be used for the internal grid points located far from the boundary and 27-point non-uniform stencils that will be used for the grid points located close to the boundary. Let us consider a 3-D bounded domain and a Cartesian rectangular mesh with the mesh size h where h is the size of the mesh along the x-axis,  $b_y h$  and  $b_z h$  are the sizes of the mesh along the y- and z-axes ( $b_y$  and  $b_z$  are the aspect ratios of the mesh); see Fig. 1. The 27-point stencil considered here is similar to that for the 3-D linear quadrilateral finite elements. The spatial locations of the 26 degrees of freedom that are close to the internal degree of freedom  $u_{A,B,C}$  and contribute to the 27-point stencil for this degree of freedom are shown in Fig. 1 for the case when the boundary and the Cartesian mesh are matched or when the degree of freedom  $u_{A,B,C}$  is located far from the boundary. In the case of non-matching grids when the grid points do not coincide with the boundary, the grid points that contribute to the stencil for the internal point  $u_{A,B,C}$  and are located outside the physical domain are moved to the boundary of the physical domain as shown in Fig. 2. They form 27-point nonuniform stencils for the internal grid points  $u_{14}$  ( $u_{A,B,C}$ ) located close to the boundary. For convenience, the local numeration of the grid points from 1 to 27 is used in Fig. 2 as well as in the derivations below for the 27-point uniform and non-uniform stencils. In order to find the boundary points that are included into the stencil for the degree of freedom  $u_{14}$  (see Fig. 2) we join the central point  $u_{14}$  with the 26 closest grid points of the Cartesian mesh; i.e., we have 26 straight lines starting from point  $u_{14}$ . If any of these lines intersects the boundary of the domain then the corresponding

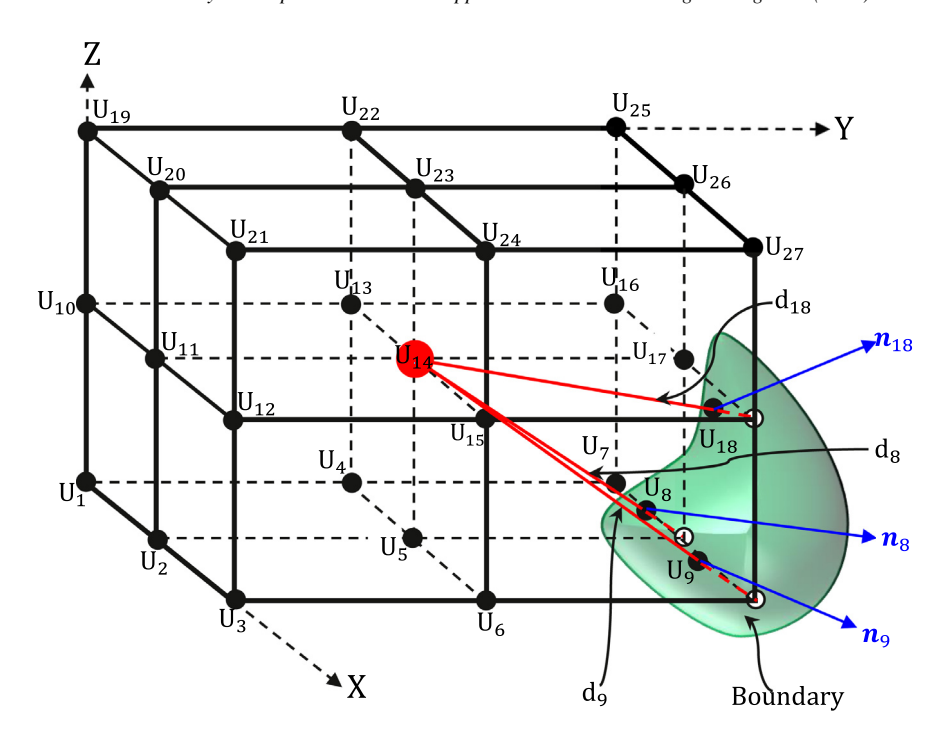


Fig. 2. The spatial locations of the degrees of freedom  $u_p$  ( $p=1,2,\ldots,27$ ) that contribute to the 27-point nonuniform stencil for the internal degree of freedom  $u_{14}$  located close to the boundary.

grid points of the Cartesian mesh should be moved to the boundary. E.g., Fig. 2 shows a particular case when only 3 lines out of 26 intersect the boundary and three grid points  $u_8$ ,  $u_9$  and  $u_{18}$  (designated as  $\circ$ ) are moved to the boundary (the new locations are designated as  $\bullet$ ). In our approach, for all internal points located within the domain we use 27-point uniform (see Fig. 1) or non-uniform (see Fig. 2) stencils. In order to describe the coordinates of the boundary points for non-uniform stencils, we introduce 27 coefficients  $0 \le d_p \le 1$  (p = 1, 2, ..., 27) as follows (see also Fig. 2):

$$x_p = x_{14} + (i-2)d_ph$$
,  $y_p = y_{14} + (j-2)d_pb_vh$ ,  $z_p = z_{14} + (k-2)d_pb_zh$ , (8)

where  $d_{14} = 0$ , p = 9(k - 1) + 3(j - 1) + i with i, j, k = 1, 2, 3. Eq. (8) can be also used for the coordinates of the grid points of the 27-point uniform stencil with the corresponding coefficients  $d_p$  equal to unity ( $d_p = 1$ ). E.g., only three coefficients  $d_8 < 1$ ,  $d_9 < 1$  and  $d_{18} < 1$  in Fig. 2 are smaller than one and all other coefficients are equal to unity,  $d_p = 1$  (p = 1, ..., 7, 10, ..., 13, 15, 16, 17, 19, ..., 27).

Eq. (4) for the 27-point uniform (see Fig. 1) or nonuniform (see Fig. 2) stencil for the grid point  $u_{14}$  (or  $u_{A,B,C}$ ) will be assumed in the following form:

$$h^{2} \sum_{p=1}^{27} m_{p} \frac{d^{n} u_{p}^{num}}{dt^{n}} + \sum_{p=1}^{27} k_{p} u_{p}^{num} = \left[h^{3} \sum_{p=1}^{27} \bar{m}_{p} \frac{d^{n} g_{1}(x_{p}, y_{p}, z_{p}, t)}{dt^{n}} + h \sum_{p=1}^{27} \bar{k}_{p} g_{1}(x_{p}, y_{p}, z_{p}, t)\right] + \bar{f}_{14}, \qquad (9)$$

where  $\bar{f}_{14}=0$  in the case of zero load (source) f=0 in Eqs. (1) and (2), the expression in the square brackets on the right-hand side of Eq. (9) is known and represents the Neumann boundary conditions with their time derivatives at the stencil points with the coordinates  $x_p$ ,  $y_p$ ,  $z_p$  that belong to the boundary with the Neumann boundary conditions (see Fig. 2), the unknown stencil coefficients  $m_p$ ,  $\bar{m}_p$ ,  $k_p$ , and  $\bar{k}_p$  ( $p=1,2,\ldots,27$ ) are to be determined from the minimization of the local truncation error,  $m_p=0$  and  $k_p=0$  if a point with the coordinates  $x_p$ ,  $y_p$ ,  $z_p$  belongs to the boundary with the Neumann boundary conditions; otherwise,  $\bar{m}_p=0$  and  $\bar{k}_p=0$  (this means that Eq. (9) includes only 54 non-zero coefficients  $m_p$ ,  $\bar{m}_p$ ,  $k_p$ , and  $\bar{k}_p$ ), the central grid point with the coordinates  $x_{14}$ ,  $y_{14}$  and  $z_{14}$  is always the internal point (therefore  $\bar{m}_{14}=0$  and  $\bar{k}_{14}=0$ ), the superscript n in the time derivative in Eq. (9) is n=1 for the heat equation and n=2 for the wave equation.

**Remark 1.** Only 53 out of the 54 coefficients  $m_p$ ,  $\bar{m}_p$ ,  $k_p$ , and  $\bar{k}_p$  ( $p=1,2,\ldots,27$ ) in Eq. (9) can be considered as unknown coefficients. This can be explained as follows. In the case of zero load (source) f=0 and  $\bar{f}_{14}=0$ , Eq. (9) can be rescaled by the division of the left and right sides of Eq. (9) by any non-zero scalar  $a_1$ . For example, let us select  $a_1=k_{14}$ . In this case the rescaled coefficients of the stencil equation are:  $m_p/k_{14}$ ,  $\bar{m}_p/k_{14}$ ,  $\bar{k}_p/k_{14}$  ( $p=1,2,\ldots,27$ ),  $k_{14}=1$ ,  $k_p/k_{14}$  ( $p=1,2,\ldots,13,15,\ldots,27$ ); i.e., there is only 53 unknown rescaled coefficients. The case of nonzero load (source)  $\bar{f}_{14}\neq 0$  can be similarly treated because the term  $\bar{f}_{14}$  is a linear function of the stencil coefficients (see Eq. (24)).

**Remark 2.** The stencil equations for the new approach are constructed only for the internal Cartesian grid points located inside the domain. There are no stencils for the boundary points; the boundary points contribute to the stencils of the internal points; see the right-hand side of Eq. (9). The form of the 27-point stencils in Eq. (9) provides a high order accuracy for uniform and non-uniform stencils for the internal grid points located close to the boundary with the Neumann boundary conditions.

The local truncation error e of the stencil equation, Eq. (9), at any time t can be written down by the replacement of the numerical solution in Eq. (9) by the exact solution as follows:

$$e = h^{2} \sum_{p=1}^{27} m_{p} \frac{\partial^{n} u_{p}}{\partial t^{n}} + \sum_{p=1}^{27} k_{p} u_{p} - h^{3} \sum_{p=1}^{27} \bar{m}_{p} (n_{1p} \frac{\partial^{n+1} u_{p}}{\partial x \partial t^{n}} + n_{2p} \frac{\partial^{n+1} u_{p}}{\partial y \partial t^{n}} + n_{3p} \frac{\partial^{n+1} u_{p}}{\partial z \partial t^{n}})$$

$$- h \sum_{p=1}^{27} \bar{k}_{p} (n_{1p} \frac{\partial u_{p}}{\partial x} + n_{2p} \frac{\partial u_{p}}{\partial y} + n_{3p} \frac{\partial u_{p}}{\partial z}) - \bar{f}_{14}, \qquad (10)$$

where  $n_{1p}$ ,  $n_{2p}$  and  $n_{3p}$  (p = 1, 2, ..., 27) are the x-, y- and z-components of the outward unit normal vector  $\mathbf{n}_p$  at the boundary point p (see Fig. 2), function u(x, y, z, t) in Eq. (10) corresponds to the exact solution, the Neumann boundary conditions on the right-hand side of Eq. (9) are expressed in terms of the function u(x, y, z, t) and are moved to the left-hand side of Eq. (10). In order to represent the local truncation error e as a Taylor series, let us expand the exact solution to the wave or heat equation in Eq. (10) into a Taylor series at small  $h \ll 1$  as follows:

$$u_{p} = u_{14} + \frac{\partial u_{14}}{\partial x} [(i-2)d_{p}h] + \frac{\partial u_{14}}{\partial y} [(j-2)d_{p}b_{y}h] + \frac{\partial u_{14}}{\partial z} [(k-2)d_{p}b_{z}h] + \frac{\partial^{2}u_{14}}{\partial x^{2}} \frac{[(i-2)d_{p}h]^{2}}{2!}$$

$$+ \frac{\partial^{2}u_{14}}{\partial y^{2}} \frac{[(j-2)d_{p}b_{y}h]^{2}}{2!} + \frac{\partial^{2}u_{14}}{\partial z^{2}} \frac{[(k-2)d_{p}b_{z}h]^{2}}{2!} + 2\frac{\partial^{2}u_{14}}{\partial x\partial y} \frac{[(i-2)d_{p}h][(j-2)d_{p}b_{y}h]}{2!}$$

$$+ 2\frac{\partial^{2}u_{14}}{\partial x\partial z} \frac{[(i-2)d_{p}h][(k-2)d_{p}b_{z}h]}{2!} + 2\frac{\partial^{2}u_{14}}{\partial y\partial z} \frac{[(j-2)d_{p}b_{y}h][(k-2)d_{p}b_{z}h]}{2!} + \cdots,$$

$$(11)$$

$$\frac{\partial u_p}{\partial s} = \frac{\partial u_{14}}{\partial s} + \frac{\partial^2 u_{14}}{\partial s \partial x} [(i-2)d_p h] + \frac{\partial^2 u_{14}}{\partial s \partial y} [(j-2)d_p b_y h] + \frac{\partial^2 u_{14}}{\partial s \partial z} [(k-2)d_p b_z h] + \frac{\partial^3 u_{14}}{\partial s \partial x^2} \frac{[(i-2)d_p h]^2}{2!} \\
+ \frac{\partial^3 u_{14}}{\partial s \partial y^2} \frac{[(j-2)d_p b_y h]^2}{2!} + \frac{\partial^3 u_{14}}{\partial s \partial z^2} \frac{[(k-2)d_p b_z h]^2}{2!} + 2 \frac{\partial^3 u_{14}}{\partial s \partial x \partial y} \frac{[(i-2)d_p h][(j-2)d_p b_y h]}{2!} \\
+ 2 \frac{\partial^3 u_{14}}{\partial s \partial x \partial z} \frac{[(i-2)d_p h][(k-2)d_p b_z h]}{2!} + 2 \frac{\partial^3 u_{14}}{\partial s \partial y \partial z} \frac{[(j-2)d_p b_y h][(k-2)d_p b_z h]}{2!} + \cdots, \tag{12}$$

where  $\frac{\partial}{\partial s} = \frac{\partial^n}{\partial t^n}$ ,  $\frac{\partial}{\partial s} = \frac{\partial}{\partial x}$ ,  $\frac{\partial}{\partial s} = \frac{\partial}{\partial y}$ ,  $\frac{\partial}{\partial s} = \frac{\partial}{\partial z}$ ,  $\frac{\partial}{\partial s} = \frac{\partial}{\partial z}$ ,  $\frac{\partial}{\partial s} = \frac{\partial^{n+1}}{\partial x \partial t^n}$ ,  $\frac{\partial}{\partial s} = \frac{\partial^{n+1}}{\partial y \partial t^n}$ ,  $\frac{\partial}{\partial s} = \frac{\partial^{n+1}}{\partial z \partial t^n}$ , and p = 9(k-1) + 3(j-1) + i with i, j, k = 1, 2, 3; see Fig. 2. The exact solution  $u_{14}$  to the wave and heat equations, Eqs. (1) and (2) with f = 0 at  $x = x_{14}$ ,  $y = y_{14}$  and  $z = z_{14}$  meets the following equations:

$$\frac{\partial^n u_{14}}{\partial t^n} - \bar{c} \nabla^2 u_{14} = 0, \tag{13}$$

$$\frac{\partial^{(i+j+k+n)} u_{14}}{\partial x^i \partial y^j \partial z^k \partial t^n} - \bar{c} \frac{\partial^{(i+j+k)} \nabla^2 u_{14}}{\partial x^i \partial y^j \partial z^k} = 0, \tag{14}$$

with  $\bar{c} = c^2$  for the wave equation and  $\bar{c} = a$  for the heat equation as well as  $i, j, k = 0, 1, 2, 3, 4, \ldots$  Here, Eq. (14) is directly obtained by the differentiation of Eq. (13) with respect to x, y and z. Inserting Eqs. (11)–(14)

with the exact solution into Eq. (10) we will get the following local truncation error in space e:

$$e = \bar{c}\{b_1u_{14} + h[b_2\frac{\partial u_{14}}{\partial x} + b_3\frac{\partial u_{14}}{\partial y} + b_4\frac{\partial u_{14}}{\partial z}] + h^2[b_3\frac{\partial^2 u_{14}}{\partial x^2} + b_6\frac{\partial^2 u_{14}}{\partial x\partial y} + b_7\frac{\partial^2 u_{14}}{\partial x\partial z} + b_7\frac{\partial^2 u_{14}}{\partial x\partial z}]$$

$$+ b_8\frac{\partial^2 u_{14}}{\partial y^2} + b_9\frac{\partial^2 u_{14}}{\partial y\partial z} + b_{10}\frac{\partial^2 u_{14}}{\partial x^2\partial y} + b_{13}\frac{\partial^3 u_{14}}{\partial x^2\partial z} + b_{14}\frac{\partial^3 u_{14}}{\partial x\partial y^2} + b_{15}\frac{\partial^3 u_{14}}{\partial x\partial y^2} + b_{16}\frac{\partial^3 u_{14}}{\partial x\partial y^2} + b_{16}\frac{\partial^3 u_{14}}{\partial x\partial z^2} + b_{19}\frac{\partial^3 u_{14}}{\partial y^2 z^2} + b_{20}\frac{\partial^3 u_{14}}{\partial z^3} + b_{15}\frac{\partial^3 u_{14}}{\partial x^2 \partial y^2} + b_{25}\frac{\partial^4 u_{14}}{\partial x^2 \partial y^2} + b_{25}\frac{\partial^4 u_{14}}{\partial x^2 \partial y^2} + b_{26}\frac{\partial^4 u_{14}}{\partial x^2 \partial y^2} + b_{26}\frac{\partial^4 u_{14}}{\partial x^2 \partial z^2} + b_{26}\frac{\partial^4 u_{14}}{\partial x^2 \partial y^2} + b$$

where the coefficients  $b_p$  ( $p=1,2,\ldots$ ) are expressed in terms of the coefficients  $m_j$  and  $k_j$  ( $j=1,2,\ldots,27$ ); see Appendix A. Due to Eqs. (13) and (14), there are no time derivatives in Eq. (15). For the uniform stencil in Fig. 1 with  $d_p=1$  ( $p=1,2,\ldots,13,15,\ldots,27$ ) the expressions for coefficients  $b_p$  ( $p=1,2,\ldots$ ) are simplified and some results can be obtained analytically. For example, equating to zero coefficients  $b_p$  ( $p=1,2,\ldots,35$ ) up to the fourth order in Eq. (15) yields all zero coefficients  $k_p$  and  $\bar{k}_p$  ( $p=1,2,\ldots,27$ ) in the stencil equation after the solution of the corresponding system of algebraic equations  $b_p=0,\ p=1,2,\ldots,35$ . This means that we cannot generally zero all first 35 coefficients  $b_p$  in Eq. (15). In order to improve the order of the local truncation error in Eq. (15) for uniform and non-uniform stencils at small  $h\ll 1$ , we will zero the first 20 coefficients  $b_p$  in Eq. (15) up to the third order with respect to h; i.e.,

$$b_p = 0, p = 1, 2, \dots, 20.$$
 (16)

Then, in order to have a sufficient number of linearly independent equations for the calculation of the stencil coefficients  $m_p$ ,  $\bar{m}_p$ ,  $k_p$ , and  $\bar{k}_p$  ( $p=1,2,\ldots,27$ ) in Eq. (9), we use the least square method for the minimization of coefficients  $b_p$  related to the fourth and higher orders of the local truncation error with the following

residual R:

$$R = \sum_{p=21}^{35} b_p^2 + h_1 \sum_{p=36}^{56} b_p^2 + h_2 \sum_{p=57}^{84} b_p^2 + h_3 \sum_{p=85}^{120} b_p^2 + h_4 \sum_{p=121}^{165} b_p^2,$$
(17)

where  $h_i$  (i = 1, 2, 3, 4) are the weighting factors to be selected (e.g., the numerical experiments show that  $h_i = 1$  (i = 1, 2, 3, 4) yields accurate results). In order to minimize the residual R with the constraints given by Eq. (16), we can form a new residual  $\bar{R}$  with the Lagrange multipliers  $\lambda_R$ :

$$\bar{R} = \sum_{p=1}^{20} \lambda_p b_p + \sum_{p=21}^{35} b_p^2 + h_1 \sum_{p=36}^{56} b_p^2 + h_2 \sum_{p=57}^{84} b_p^2 + h_3 \sum_{p=85}^{120} b_p^2 + h_4 \sum_{p=121}^{165} b_p^2.$$
 (18)

The residual  $\bar{R}$  is a quadratic function of coefficients  $m_p$ ,  $\bar{m}_p$ ,  $k_p$ ,  $\bar{k}_p$  ( $p=1,2,\ldots,27$ ) and a linear function of the Lagrange multipliers  $\lambda_p$ ; i.e.,  $\bar{R}=\bar{R}(m_p,k_p,\bar{m}_p,\bar{k}_p,\lambda_p)$ . In order minimize the residual  $\bar{R}(m_p,k_p,\bar{m}_p,\bar{k}_p,\lambda_p)$ , the following equations based on the least square method for the residual  $\bar{R}$  can be written down:

$$\frac{\partial \bar{R}}{\partial m_p} = 0, \qquad \frac{\partial \bar{R}}{\partial k_p} = 0, \qquad \frac{\partial \bar{R}}{\partial \bar{m}_p} = 0, \qquad \frac{\partial \bar{R}}{\partial \bar{k}_p} = 0, \qquad p = 1, 2, \dots, 27, \tag{19}$$

$$\frac{\partial \bar{R}}{\partial \lambda_p} = 0, \qquad p = 1, 2, \dots, 20, \tag{20}$$

where equation  $\frac{\partial \bar{k}}{\partial k_{14}} = 0$  should be replaced by  $k_{14} = 1$ ; see Remark 1 after Eq. (9). Eqs. (19) and (20) form a system of 74 linear algebraic equations with respect to 54 unknown coefficients  $m_p$ ,  $\bar{m}_p$ ,  $k_p$ ,  $\bar{k}_p$ , p = 1, 2, ..., 27 (one of the coefficients  $m_p$  or  $\bar{m}_p$  and  $k_p$  or  $\bar{k}_p$  is always zero and we should exclude the corresponding equations in Eq. (19); see the explanations after Eq. (9)) and 20 Lagrange multipliers  $\lambda_p$  (p = 1, 2, ..., 20). Solving these linear algebraic equations numerically, we can find the coefficients  $m_p$ ,  $\bar{m}_p$ ,  $k_p$ ,  $\bar{k}_p$  (p = 1, 2, ..., 27) for the 27-point uniform and non-uniform stencils. As can be seen from the procedure, the 27-point stencil provides the fourth order of the local truncation error in Eq. (15). This is one order less accurate than the fifth order of the local truncation error of the new approach for the Dirichlet boundary conditions developed in [31] but is one order more accurate than the order of the local truncation error for the linear finite elements with similar stencils. Moreover, due to the minimization of the leading fourth order terms of the local truncation error in Eq. (18), at the same numbers of degrees of freedom the new approach yields more accurate results than those obtained by the high-order finite elements (up to the fourth order) with much wider stencils; see the numerical examples below.

**Remark 3.** To estimate the computation costs of the solution of 74 linear algebraic equations formed by Eqs. (19) and (20) we solved  $10^6$  such systems with a general MATLAB solver on a simple student laptop computer (Processor: Intel (R) Core(TM) i5-4210U CPU @ 1.70 GHz 2.40 GHz). The computation 'wall' time was T=7356 s for  $10^6$  systems or the average time for one system was 0.007356 s. Because the coefficients  $m_p$ ,  $\bar{m}_p$ ,  $k_p$ ,  $\bar{k}_p$ ,  $p=1,2,\ldots,27$  are independently calculated for different non-uniform stencils, the computation time of their calculation for different grid points can be significantly reduced on modern parallel computers. This means that for large global systems of equations, the computation time for the calculation of the coefficients  $m_p$ ,  $\bar{m}_p$ ,  $k_p$ ,  $\bar{k}_p$ ,  $p=1,2,\ldots,27$  is very small compared to that for the solution of the global system of equations.

Remark 4. The proposed technique yields accurate results for the non-uniform stencils even with very small coefficients  $d_i \ll 1$ ; see below the numerical examples. However, the new technique allows also to exclude very small coefficients  $d_i \ll 1$  from calculations. For example, if  $d_i \ll tol$  for some internal point where tol is a small tolerance (e.g.,  $tol = 10^{-3}$ ), then the non-uniform stencil for this internal point can be removed from the global system of equations and this point can be moved to the boundary and treated as the boundary point for other stencils. In this case, the corresponding coefficients  $d_i$  for this point in other stencils can be slightly greater than one. According to the derivations in the previous Section, all equations will be valid also for  $d_i > 1$ . The numerical experiments with a small tolerance  $tol = 10^{-3}$  show that if the point with very small coefficients  $d_i \ll 1$  is moved to the boundary then the coefficients  $d_i$  for this point in other stencils can be taken as  $d_i = 1$  without introducing any significant errors.

**Remark 5.** The 27-point stencil equations for the internal grid points as well as for the grid points close to the boundary with the Dirichlet boundary conditions can be obtained from Eq. (9) with the coefficients  $\bar{m}_p = \bar{k}_p = 0$  (p = 1, 2, ..., 27). The corresponding derivations are presented in our paper [31].

The final semi-discrete system of equations includes the 27-point uniform and nonuniform stencil equations (see Figs. 1 and 2) for all internal grid points located inside the domain and close to the boundary with the Dirichlet boundary conditions (see [31]) as well as the 27-point uniform and nonuniform stencil equations for all internal grid points located close to the boundary with the Neumann boundary conditions (see Figs. 1 and 2 and Eq. (9)). It is interesting to note that the final semi-discrete system of equations does not include the unknowns at the boundary; i.e., all unknowns are introduced at the internal grid points and the Neumann boundary conditions can be considered as the known load (source) term for the final global system of equations.

# 2.2. Nonzero load (source) $f \neq 0$ in Eqs. (1) and (2)

The inclusion of non-zero loading (source) term f in the partial differential equations, Eqs. (1) and (2), leads to the non-zero term  $\bar{f}_{14}$  in the stencil equation, Eq. (9) (similar to Eq. (4)). The expression for the term  $\bar{f}_{14}$  can be calculated from the procedure used for the derivation of the local truncation error in the case of zero loading (source) term as follows. In the case of non-zero loading (source) term ( $f(x, t) \neq 0$ ), Eqs. (13) and (14) for the exact solution at  $x = x_{14}$ ,  $y = y_{14}$  and  $z = z_{14}$  can be modified:

$$\frac{\partial^n u_{14}}{\partial t^n} - \bar{c} \nabla^2 u_{14} = f(x_{14}, y_{14}, z_{14}, t), \tag{21}$$

$$\frac{\partial^{(i+j+k+n)} u_{14}}{\partial x^i \partial y^j \partial z^k \partial t^n} - \bar{c} \frac{\partial^{(i+j+k)} \nabla^2 u_{14}}{\partial x^i \partial y^j \partial z^k} = \frac{\partial^{(i+j+k)} f(x_{14}, y_{14}, z_{14}, t)}{\partial x^i \partial y^j \partial z^k}. \tag{22}$$

Then, inserting Eqs. (11), (12), (21) and (22) with the exact solution to the wave or heat equation, Eq. (1) or (2), into Eq. (10), we will get the following local truncation error in space  $e_f$ :

$$e_f = e - [\bar{f}_{14} - \{h^2 f_{14}(m_1 + m_2 + m_3 + \dots) + \dots\}],$$
 (23)

where e is the local truncation error in space given by Eq. (15) for zero loading (source) term,  $f_{14}$  designates function f(x, y, z, t) calculated at  $x = x_{14}$ ,  $y = y_{14}$  and  $z = z_{14}$ . Equating to zero the expression in the square brackets on the right-hand side of Eq. (23), we will get the expression for  $f_{14}$ :

$$\bar{f}_{14} = h^2 f_{14}(m_1 + m_2 + m_3 + \dots) + \dots,$$
 (24)

as well as we will get the same local truncation errors  $e_f = e$  for zero and non-zero loading (source) term (see Appendix B for the detailed expression of  $\bar{f}_{14}$ ). This means that the coefficients  $m_p$ ,  $\bar{m}_p$ ,  $k_p$ ,  $\bar{k}_p$ , p = 1, 2, ..., 27 of the stencil equations are first calculated for zero load (source) f = 0 as described in Section 2.1. Then, the nonzero loading (source) term  $\bar{f}_{14}$  given by Eq. (24) is used in the stencil equation, Eq. (9).

#### 3. A new numerical approach for the 3-D Poisson equation

# 3.1. Zero source f = 0 in Eq. (3)

The derivation of the new approach for the Poisson equation is similar to that for the wave and heat equations in Section 2. The 27-point uniform and non-uniform stencils introduced in Section 2.1 (see Figs. 1 and 2) will be used with the new approach for the internal grid points located far from the boundary and for the grid points located close to the boundary. The stencil equation for the degree of freedom  $u_{14}^{num}$  of the time independent Poisson equation can be obtained from Eq. (9) with  $m_p = 0$  and  $\bar{m}_p = 0$  for p = 1, 2, ..., 27 as follows:

$$\sum_{p=1}^{27} k_p u_p^{num} = h \sum_{p=1}^{27} \bar{k}_p g_1(x_p, y_p, z_p) + \bar{f}_{14}, \qquad (25)$$

where  $\bar{f}_{14} = 0$  in the case of zero source f = 0 in Eq. (3), the first term on the right-hand side of Eq. (25) is known and represents the Neumann boundary conditions at the stencil points with the coordinates  $x_p$ ,  $y_p$ ,  $z_p$  that belong to

the boundary with the Neumann boundary conditions, the unknown stencil coefficients  $k_p$  and  $\bar{k}_p$  ( $p=1,2,\ldots,27$ ) are to be determined from the minimization of the local truncation error,  $k_p=0$  if a point with the coordinates  $x_p, y_p, z_p$  belongs to the boundary with the Neumann boundary conditions; otherwise,  $\bar{k}_p=0$  (this means that Eq. (25) includes only 27 non-zero coefficients  $k_p$  and  $\bar{k}_p$ ), the central grid point with the coordinates  $x_{14}$ ,  $y_{14}$  and  $z_{14}$  is always the internal point (therefore  $\bar{k}_{14}=0$ ).

The exact solution  $u_{14}$  to the Poisson equation, Eq. (3), with f = 0 at  $x = x_{14}$ ,  $y = y_{14}$  and  $z = z_{14}$  meets the following equations:

$$\frac{\partial^2 u_{14}}{\partial x^2} = -\left(\frac{\partial^2 u_{14}}{\partial y^2} + \frac{\partial^2 u_{14}}{\partial z^2}\right),\tag{26}$$

$$\frac{\partial^{(2+i+j+k)}u_{14}}{\partial x^{2+i}\partial y^{j}\partial z^{k}} = -\left(\frac{\partial^{(2+i+j+k)}u_{14}}{\partial x^{i}\partial y^{(j+2)}\partial z^{k}} + \frac{\partial^{(2+i+j+k)}u_{14}}{\partial x^{i}\partial y^{j}\partial z^{(k+2)}}\right) \tag{27}$$

with  $i, j, k = 0, 1, 2, 3, 4, \ldots$  Here, Eq. (27) is directly obtained by the differentiation of Eq. (26) with respect to x, y and z. For the calculation of the local truncation error, we also use Eq. (11). Inserting Eqs. (11), (26), (27) into the stencil equation, Eq. (25), we will get the following local truncation error in space e:

$$e = b_{1}u_{14} + h\left[b_{2}\frac{\partial u_{14}}{\partial z} + b_{3}\frac{\partial u_{14}}{\partial y} + b_{4}\frac{\partial u_{14}}{\partial x}\right] + h^{2}\left[b_{5}\frac{\partial^{2}u_{14}}{\partial z^{2}} + b_{6}\frac{\partial^{2}u_{14}}{\partial y\partial z} + b_{7}\frac{\partial^{2}u_{14}}{\partial y^{2}} + b_{8}\frac{\partial^{2}u_{14}}{\partial x\partial z} + b_{9}\frac{\partial^{2}u_{14}}{\partial x\partial y}\right]$$

$$+ h^{3}\left[b_{10}\frac{\partial^{3}u_{14}}{\partial z^{3}} + b_{11}\frac{\partial^{3}u_{14}}{\partial y\partial z^{2}} + b_{12}\frac{\partial^{3}u_{14}}{\partial y^{2}\partial z} + b_{13}\frac{\partial^{3}u_{14}}{\partial y^{3}} + b_{14}\frac{\partial^{3}u_{14}}{\partial x\partial z^{2}} + b_{15}\frac{\partial^{3}u_{14}}{\partial x\partial y\partial z} + b_{16}\frac{\partial^{3}u_{14}}{\partial x\partial y^{2}}\right]$$

$$+ h^{4}\left[b_{17}\frac{\partial^{4}u_{14}}{\partial z^{4}} + b_{18}\frac{\partial^{4}u_{14}}{\partial y\partial z^{3}} + b_{19}\frac{\partial^{4}u_{14}}{\partial y^{2}\partial z^{2}} + b_{20}\frac{\partial^{4}u_{14}}{\partial y^{3}\partial z} + b_{21}\frac{\partial^{4}u_{14}}{\partial y^{4}} + b_{22}\frac{\partial^{4}u_{14}}{\partial x\partial z^{3}} + b_{23}\frac{\partial^{4}u_{14}}{\partial x\partial y\partial z^{2}}\right]$$

$$+ b_{24}\frac{\partial^{4}u_{14}}{\partial z^{2}} + b_{27}\frac{\partial^{4}u_{14}}{\partial y\partial z^{4}} + b_{28}\frac{\partial^{5}u_{14}}{\partial y^{2}\partial z^{3}} + b_{29}\frac{\partial^{5}u_{14}}{\partial y^{3}\partial z^{2}} + b_{30}\frac{\partial^{5}u_{14}}{\partial y^{4}\partial z} + b_{31}\frac{\partial^{5}u_{14}}{\partial y^{5}} + b_{32}\frac{\partial^{5}u_{14}}{\partial x\partial z^{4}}$$

$$+ b_{33}\frac{\partial^{5}u_{14}}{\partial x\partial y\partial z^{3}} + b_{34}\frac{\partial^{5}u_{14}}{\partial x\partial y^{2}\partial z^{2}} + b_{35}\frac{\partial^{5}u_{14}}{\partial x\partial y^{3}\partial z} + b_{36}\frac{\partial^{5}u_{14}}{\partial x\partial y^{3}}\right]$$

$$+ h^{6}\left[b_{37}\frac{\partial^{6}u_{14}}{\partial z^{6}} + b_{38}\frac{\partial^{6}u_{14}}{\partial y\partial z^{5}} + b_{39}\frac{\partial^{6}u_{14}}{\partial y^{2}\partial z^{4}} + b_{40}\frac{\partial^{6}u_{14}}{\partial y^{3}\partial z^{3}} + b_{41}\frac{\partial^{6}u_{14}}{\partial y^{4}\partial z^{2}} + b_{42}\frac{\partial^{6}u_{14}}{\partial y^{5}\partial z}\right]$$

$$+ b_{43}\frac{\partial^{6}u_{14}}{\partial y^{6}} + b_{44}\frac{\partial^{6}u_{14}}{\partial y^{6}} + b_{44}\frac{\partial^{6}u_{14}}{\partial x\partial y^{2}\partial z^{3}} + b_{47}\frac{\partial^{6}u_{14}}{\partial x\partial y^{3}\partial z^{2}} + b_{48}\frac{\partial^{6}u_{14}}{\partial x\partial y^{4}\partial z} + b_{49}\frac{\partial^{6}u_{14}}{\partial x\partial y^{5}}\right] + O(h^{7}),$$
(28)

where the coefficients  $b_p$  ( $p=1,2,\ldots$ ) are expressed in terms of the coefficients  $k_j$  and  $\bar{k}_j$  ( $j=1,2,\ldots,27$ ); see Appendix C. Due to Eqs. (26)–(27), there are no second and higher order partial derivatives of x in Eq. (28). In order to improve the order of the local truncation error in Eq. (28) at small  $h \ll 1$ , we will equate to zero the coefficients  $b_p$  in Eq. (28) for the smallest orders of h. The stencil equation, Eq. (25), includes 27 non-zero coefficients  $k_i$  and  $\bar{k}_i$  ( $i=1,2,\ldots,27$ ) but only 26 of them can be considered as unknown coefficients (the explanation is similar to that for the wave (heat) equation in Remark 1 after Eq. (9)). For the uniform stencil in Fig. 1 with  $d_p=1$  ( $p=1,2,\ldots,27$ ) the expressions for coefficients  $b_p$  ( $p=1,2,\ldots$ ) can be simplified and some results can be obtained analytically. For example, equating to zero the coefficients  $b_p$  ( $p=1,2,\ldots,25$ ) up to the fourth order in Eq. (28) yields all zero coefficients  $\bar{k}_p$  in the stencil equation after the solution of the corresponding system of algebraic equations  $b_p=0$ ,  $p=1,2,\ldots,25$ . This means that we cannot generally zero all first 25 coefficients  $b_p$  in Eq. (28). In order to improve the order of the local truncation error in Eq. (28) for uniform and non-uniform stencils at small  $h \ll 1$ , we will zero the first 16 coefficients  $b_p$  in Eq. (28) up to the third order:

$$b_p = 0, p = 1, 2, \dots, 16.$$
 (29)

Then, in order to have a sufficient number of linearly independent equations for the calculation of the stencil coefficients  $k_p$  and  $\bar{k}_p$  ( $p=1,2,\ldots,27$ ) in Eq. (25), we use the least square method for the minimization of

coefficients  $b_p$  related to the fourth, fifth and sixth orders of the local truncation error with the following residual R:

$$R = \sum_{p=17}^{25} b_p^2 + h_1 \sum_{p=26}^{36} b_p^2 + h_2 \sum_{p=37}^{49} b_p^2,$$
(30)

where  $h_1$  and  $h_2$  are the weighting factors to be selected (e.g., the numerical experiments show that  $h_1 = h_2 = 0.1$  yields accurate results). In order to minimize the residual R with the constraints given by Eq. (29), we can form a new residual  $\bar{R}$  with the Lagrange multipliers  $\lambda_p$ :

$$\bar{R} = \sum_{p=1}^{16} \lambda_p b_p + \sum_{p=17}^{25} b_p^2 + h_1 \sum_{p=26}^{36} b_p^2 + h_2 \sum_{p=37}^{49} b_p^2.$$
(31)

The residual  $\bar{R}$  is a quadratic function of coefficients  $k_p$  and  $\bar{k}_p$  ( $p=1,2,\ldots,27$ ) and a linear function of the Lagrange multipliers  $\lambda_p$ ; i.e.,  $\bar{R}=\bar{R}(k_p,\bar{k}_p,\lambda_p)$ . In order minimize the residual  $\bar{R}(k_p,\bar{k}_p,\lambda_p)$ , the following equations based on the least square method for the residual  $\bar{R}$  can be written down:

$$\frac{\partial \bar{R}}{\partial k_p} = 0, \qquad \frac{\partial \bar{R}}{\partial \bar{k}_p} = 0, \qquad p = 1, 2, \dots, 27, \tag{32}$$

and

$$\frac{\partial \bar{R}}{\partial \lambda_p} = 0, \qquad p = 1, 2, \dots, 16, \tag{33}$$

where equation  $\frac{\partial \bar{R}}{\partial k_{14}} = 0$  should be replaced by  $k_{14} = 1$ ; see Remark 1 after Eq. (9). Eqs. (32) and (33) form a system of 43 linear algebraic equations with respect to 27 unknown non-zero coefficients  $k_p$  and  $\bar{k}_p$   $p = 1, 2, \ldots, 27$  (one of the coefficients  $k_p$  or  $\bar{k}_p$  is always zero and we should exclude the corresponding equations in Eq. (32); see the explanations after Eq. (9)) and 16 Lagrange multipliers  $\lambda_p$   $(p = 1, 2, \ldots, 16)$ . Solving these linear algebraic equations numerically, we can find the coefficients  $k_p$  and  $\bar{k}_p$   $(p = 1, 2, \ldots, 27)$  for the 27-point uniform and non-uniform stencils. As can be seen from the procedure, the 27-point stencil provides the fourth order of the local truncation error in Eq. (28). This is one order less accurate than the fifth order of the local truncation error of the new approach for the Dirichlet boundary conditions developed in [31] but is one order more accurate than the order of the local truncation error for the linear finite elements with similar stencils. Moreover, due to the minimization of the leading fourth order terms of the local truncation error in Eq. (31), at the same numbers of degrees of freedom the new approach yields more accurate results than the high-order finite elements (up to the fourth order) with much wider stencils; see the numerical examples below.

**Remark 6.** The 27-point stencil equations for the internal grid points as well as for the grid points close to the boundary with the Dirichlet boundary conditions can be obtained from Eq. (25) with the coefficients  $\bar{k}_p = 0$  (p = 1, 2, ..., 27). The corresponding derivations are presented in our paper [31].

The final semi-discrete system of equations includes the 27-point uniform and nonuniform stencil equations (see Figs. 1 and 2) for all internal grid points that are located inside the domain and close to the boundary with the Dirichlet boundary conditions (see [31]) as well as the 27-point uniform and nonuniform stencil equations for all internal grid points that are located close to the boundary with the Neumann boundary conditions (see Figs. 1 and 2 and Eq. (25)).

# 3.2. Nonzero source $f \neq 0$ in Eq. (3)

The inclusion of non-zero source term f in the partial differential equation, Eq. (3), leads to the non-zero term  $\bar{f}_{14}$  in the stencil equation, Eq. (25). The expression for the term  $\bar{f}_{14}$  can be calculated from the procedure similar to that for the wave (heat) equation in Section 2.2 and is given in Appendix D. Similar to Section 3.1, the coefficients of the stencil equations are first calculated for zero source f = 0. Then, the nonzero source term  $\bar{f}_{14}$  is used in the stencil equation, Eq. (25). The expressions for the local truncation error are the same for zero and non-zero source functions.

# 4. Numerical examples

In this Section the computational efficiency of the new approach developed in the previous Sections will be demonstrated and compared with the 3-D conventional linear and high-order finite elements. Similar to the finite element terminology, a grid point of a Cartesian mesh will be called a node. In order to compare the accuracy of the new technique with FEM, the following errors are used in the numerical examples considered below. The relative errors  $e_u^j$  for the function u and  $e_v^j$  for its first time derivative v at the jth node are defined as:

$$e_u^j = \frac{|u_j^{num} - u_j^{exact}|}{u_{max}^{exact}}$$
 and  $e_v^j = \frac{|v_j^{num} - v_j^{exact}|}{v_{max}^{exact}}$ ,  $j = 1, 2, ..., N$ . (34)

The maximum relative errors  $e_u^{max}$  for the function and  $e_v^{max}$  for its first time derivative are defined as:

$$e_u^{max} = \max_j e_u^j$$
 and  $e_v^{max} = \max_j e_v^j$ ,  $j = 1, 2, ..., N$ . (35)

In Eqs. (34)–(35) the superscripts 'num' and 'exact' correspond to the numerical and exact solutions, N is the total number of the grid points used in calculations,  $u_{max}^{exact}$  and  $v_{max}^{exact}$  are the maximum absolute values of the exact solution over the entire domain for the function and its first time derivative, respectively. For the time dependent wave and heat equations, the errors given by Eqs. (34)–(35) are evaluated at the final observation time T. The errors  $e_v^j$  and  $e_v^{max}$  are used for the wave equation only. For the time integration, the trapezoidal rule is used for the wave equation and the backward difference method is used for the heat equation. A sufficiently small size of time steps is used in calculations. In this case the error in time can be neglected and the numerical error is related to the space-discretization error only. For convenience, the function u is called 'temperature' for the heat and Poisson equations and 'displacement' for the wave equation.

In order to study the effect of matched and non-matched meshes on the accuracy of the new approach in the 3-D case, first a simple rectangular parallelepiped ABCDOPQR with the dimensions  $1 \times 1 \times 0.8$  is considered with matched and non-matched Cartesian meshes; see Fig. 3a. Then the new approach is applied to a 3-D complex irregular domain presented by a prism ABCDOPQR with a spherical hole; see Fig. 5a.

The 3-D problems for the irregular domain are also solved by the tetrahedral linear and high-order finite elements (e.g., see Fig. 6 for an example of a tetrahedral mesh) using the commercial software COMSOL.

#### 4.1. 3-D wave equation

Here, first we consider two test problems for the wave equation on regular and irregular domains with the following exact solutions:

$$u(x, y, z, t) = \sin(\beta_1 x)\sin(\beta_2 y)\sin(\beta_3 z)\cos(\beta_4 t) \tag{36}$$

with  $\beta_1 = \beta_2 = \beta_3 = 5\pi$ ,  $\beta_4 = 5\sqrt{3}\pi$  and zero loading function f = 0, and

$$u(x, y, z, t) = \sin(\beta_5 x)\cos(\beta_6 y)\sin(\beta_7 z)\cos(\beta_8 t)$$
(37)

with  $\beta_5 = \beta_8 = 5\pi$ ,  $\beta_6 = \beta_7 = 4\pi$  and non-zero loading function  $f(x, y, z, t) = (-\beta_8^2 + c^2(\beta_5^2 + \beta_6^2 + \beta_7^2))\sin(\beta_5 x)\cos(\beta_6 y)\sin(\beta_7 z)\cos(\beta_8 t)$ . The wave velocity c=1 and the observation times T=0.2 for zero loading and T=0.25 for non-zero loading are selected. For these problems, the initial conditions at time t=0 in the entire domain and the combined Neumann and Dirichlet boundary conditions along the entire boundaries are applied according to the exact solutions, Eqs. (36) and (37).

# 4.1.1. A rectangular parallelepiped

First, let us analyze the effect of matched and non-matched cubic ( $b_y = b_z = 1$ ) Cartesian meshes on the accuracy of the numerical results obtained by the new approach on the rectangular parallelepiped ABCDOPQR (see Fig. 3) with the exact solution given by Eq. (36). The Dirichlet boundary conditions are imposed on all faces except the face OPQR where the Neumann boundary conditions are imposed. In order to create a simple non-matched Cartesian mesh of size h, we use a matched Cartesian mesh of size h for the rectangular parallelepiped and then move the upper face OPQR of the rectangular parallelepiped in the z direction by a distance  $\xi h$  ( $0 \le \xi \le 1$ ) with respect to the fixed Cartesian mesh; see Fig. 3b. In this case, the height H of the parallelepiped is changed

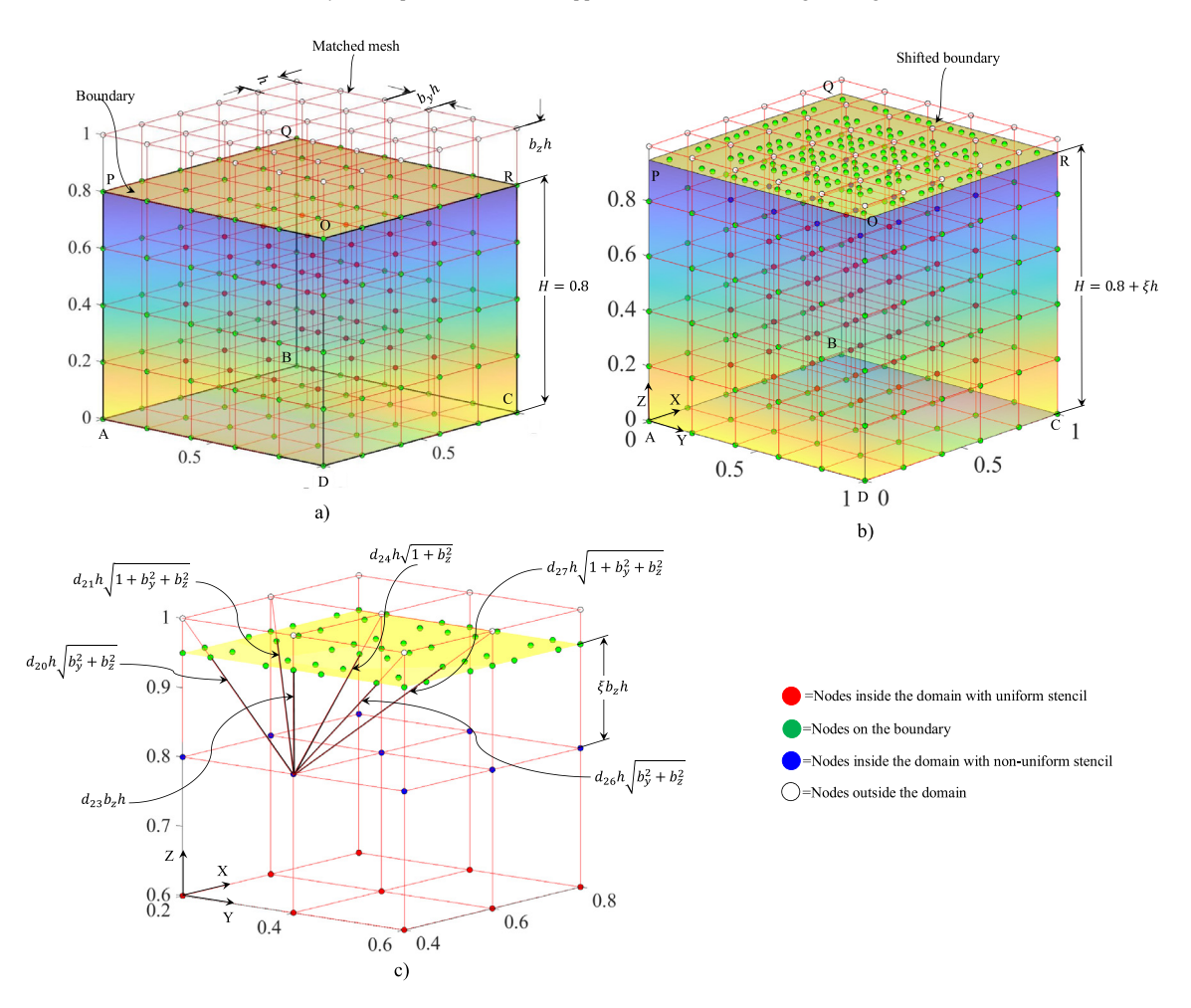


Fig. 3. A rectangular parallelepiped ABCDOPQR with matched (a) and non-matched (b) Cartesian meshes of size h and the aspect ratios  $b_v$  and  $b_{\bar{z}}$ . (c) zooms a part of the non-matched mesh (b) located close to the upper boundary OPQR.

from 0.8 to  $0.8 + \xi h$ . The 27-point stencils for the grid points located close to the upper boundary include 18 grid points inside the parallelepiped and 9 boundary points on the upper face with the Neumann boundary conditions (see Fig. 3(b,c)). For non-matched meshes, the coordinates of these boundary points are calculated according to the procedure described in Section 2.1 (see also Fig. 2). The corresponding coefficients  $d_i$  (i = 1, 2, ..., 27) used for the nonuniform stencils close to the upper boundary OPQR are:

$$d_1=d_2=\cdots=d_{13}=1\,,\;d_{14}=0\,,\;d_{15}=d_{16}=d_{17}=d_{18}=1\,,\;d_{19}=d_{20}=\cdots=d_{27}=\xi$$
 with  $0\leq\xi\leq1.$ 

**Remark 7.** Despite the fact that for the matched and non-matched meshes we consider the rectangular parallelepiped with slightly different heights, the exact solutions for these rectangular parallelepipeds are the same and are given by Eq. (36). This allows us to estimate the effect of parameter  $\xi$  of the non-matched meshes with the selected element size h on the accuracy of numerical results.

Fig. 4 shows the logarithm of the maximum relative errors in displacement  $e_u^{max}$  and in velocity  $e_v^{max}$  as a function of  $\xi$  at the selected mesh sizes h=1/10 and h=1/20. As can be seen from Fig. 4(a, c)  $e_u^{max}$  and  $e_v^{max}$  are almost constant in the range  $0.1 \le \xi \le 0.5$  and become slightly greater in the range  $0.5 \le \xi \le 1$ . At very small  $10^{-9} \le \xi \le 10^{-3}$  these errors are almost constant (see Fig. 4(b, d)). There is a small variation of  $e_u^{max}$  and  $e_v^{max}$  in

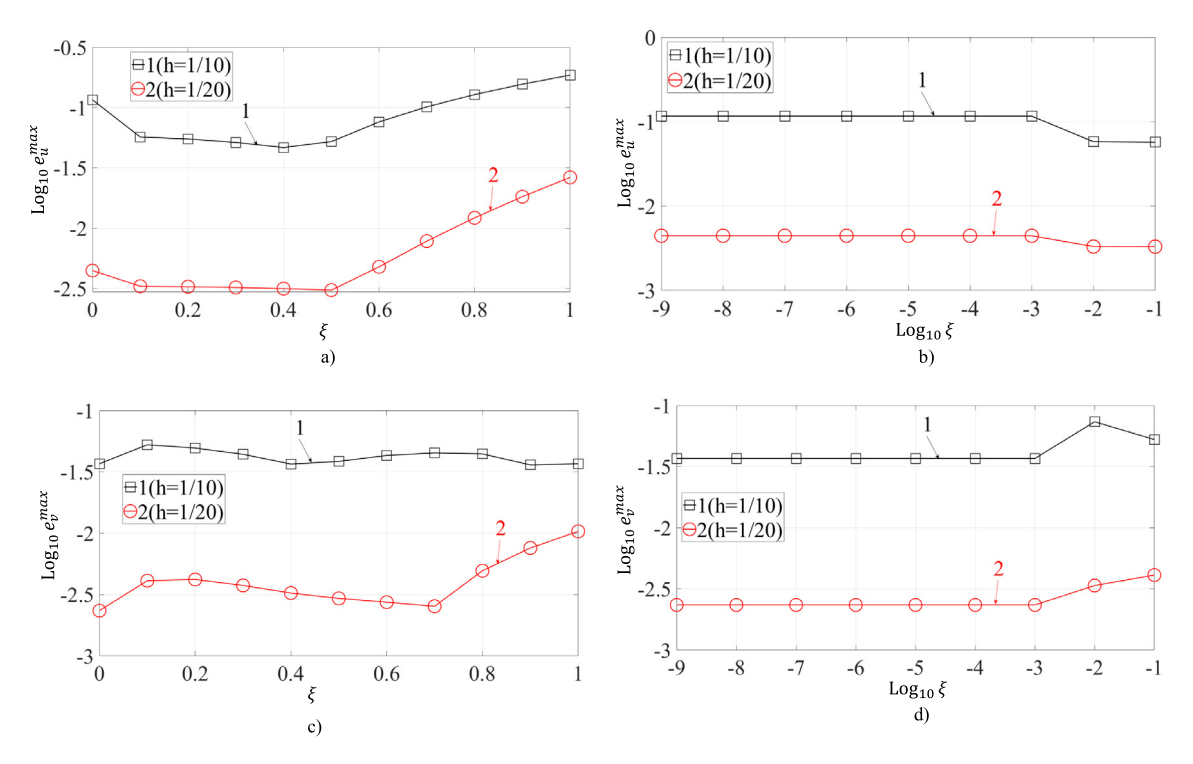


Fig. 4. The logarithm of the maximum relative errors in displacement  $e_u^{max}$  (a, b) and in velocity  $e_v^{max}$  (c, d) as a function of the coefficient  $\xi$  (a, c) and  $\log_{10}\xi$  for small  $\xi$  (b, d). The numerical solutions of the 3-D wave equation with zero loading function for the rectangular parallelepiped (see Fig. 3) are obtained by the new approach on cubic ( $b_y = b_z = 1$ ) Cartesian meshes of sizes h = 1/10 (curve 1) and h = 1/20 (curve 2). (b, d) zoom (a, c) along the x-axis for  $0 \le \xi \le 0.1$ . Symbols  $\square$  and  $\square$  correspond to the results for the different coefficients  $\xi$  used in the calculations.

the range  $10^{-3} \le \xi \le 10^{-1}$ ; see Fig. 4(b, d). These observations indicate that there is no degradation in accuracy of the new approach at very small distances  $\xi h$  between the boundary points and the internal grid points included into the stencil; i.e., in contrast the finite elements, the large differences in distances between the points included into the non-uniform stencil do not worsen the accuracy of the new approach.

# 4.1.2. A prism with a spherical hole (with the exact solutions given by Eqs. (36) and (37))

Next, let us analyze the accuracy of the new approach applied to a more complex irregular domain represented by a prism ABCDOPQR with a spherical hole; see Fig. 5a. Two problems for the 3-D wave equation with zero and non-zero loadings are solved by the new approach on the irregular domain. The Neumann boundary conditions are imposed on the upper face ROPQ and on the spherical surface of the hole whereas the Dirichlet boundary conditions are imposed on all other faces; see Fig. 5a. An example of a cubic ( $b_y = b_z = 1$ ) Cartesian mesh used with the new approach is shown in Fig. 5b.

Fig. 7 presents the errors  $e_u^{max}$  and  $e_v^{max}$  as a function of the number of degrees of freedom N in the logarithmic scale obtained by the new approach (curves 1) and by the conventional finite elements (curves 2–5) at mesh refinement. The slopes of curves 1 at large N in Fig. 7 approximately describe the order of accuracy of the new approach because  $\sqrt[3]{N}$  is approximately proportional to mesh size h (this is strictly valid for regular domain with matched meshes). As can be seen from Fig. 7, the new approach yields the order of accuracy which exceeds three for zero and non-zero loadings. This is in agreement with the theoretical results of Section 2.

Curves 2–5 in Fig. 7 present the errors  $e_u^{max}$  and  $e_v^{max}$  for the tetrahedral linear and high-order finite elements (see Fig. 6 for an example of a tetrahedral finite element mesh for the prism with the spherical hole). It can be seen from Fig. 7 that at the same N the new approach yields more accurate results than those obtained by the conventional linear and high-order (up to the fourth order) finite elements. It is important to mention that the high-order finite elements have much wider stencils and require much more computation time compared to that for the new approach

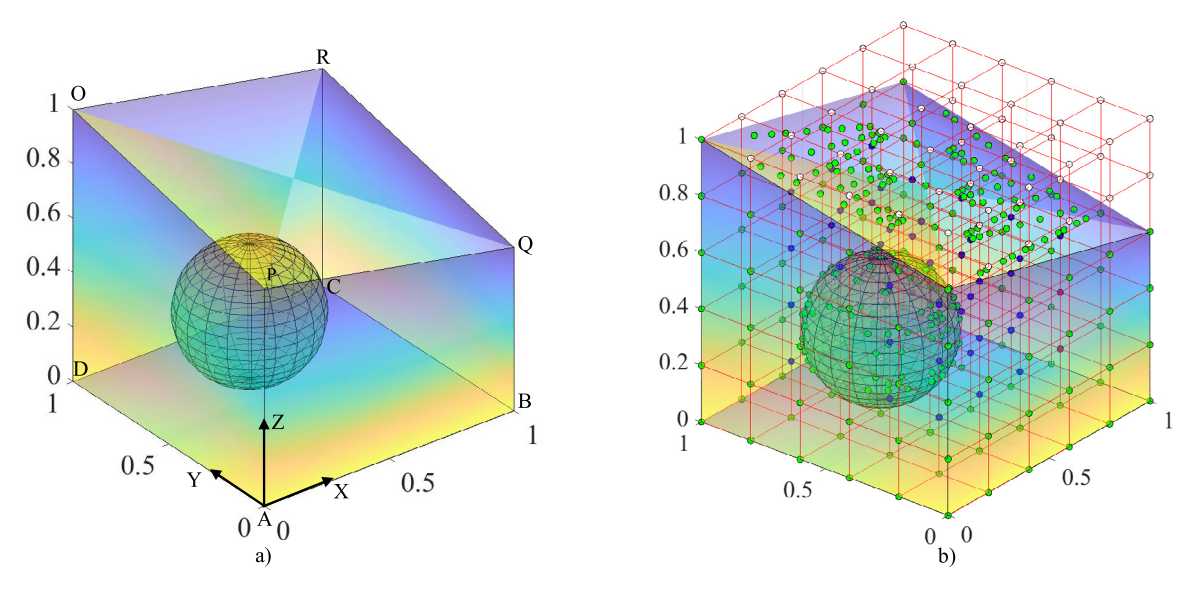


Fig. 5. (a) A 3-D prism ABCDOPQR (A(0,0,0), B(1,0,0), C(1,1,0), D(0,1,0), D(0,1,0), P(0,0,0.8), Q(1,0,0.6), R(1,1,0.8)) with a spherical hole of radius 0.25 centered at (0.4, 0.6, 0.3). b) A cubic Cartesian mesh for the new approach.

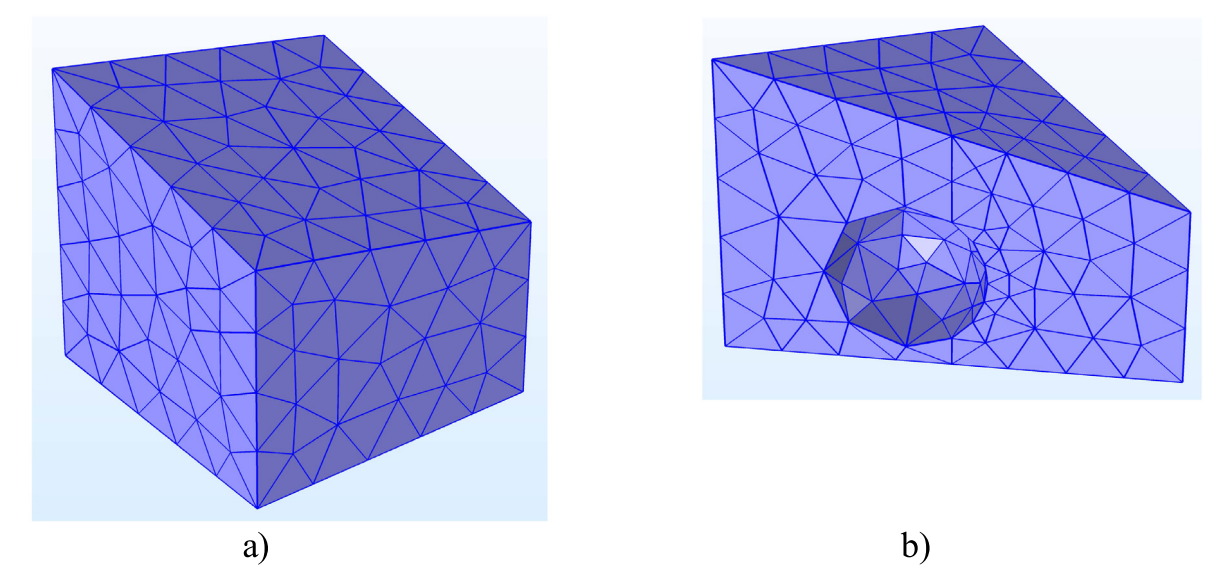


Fig. 6. (a) An example of a tetrahedral finite element mesh generated by the commercial software COMSOL for the discretization of the 3-D prism *ABCDOPQR* with the spherical hole (see Fig. 5a). b) shows a part of the mesh in the vicinity of the spherical hole.

at the same N. It is also interesting to note that at accuracy of 1%, the new approach reduces the number of degrees of freedom by a factor of greater than 1000 compared to that for the linear finite elements with similar stencils (e.g., compare curves 1 and 2 in Fig. 7c at  $\text{Log}_{10}e_u^{max}=-2$ ). This leads to a huge reduction in computation time for the new approach at a given accuracy. This reduction in computation time will be even greater if a higher accuracy is needed.

In order to study the convergence and numerical stability of the new approach in more detail, Fig. 8a presents the variation of the errors  $e_u^{max}$  and  $e_v^{max}$  at the variation of the grid size h of a Cartesian mesh with small increments  $\Delta h = \frac{1}{N_x - 1}$  where  $N_x$  is the number of the grid points along AB ( $N_x = 11, 12, ..., 31$ ); see Fig. 5a. Curve 1 in Fig. 8a corresponds to curve 1 in Fig. 7c. As can be

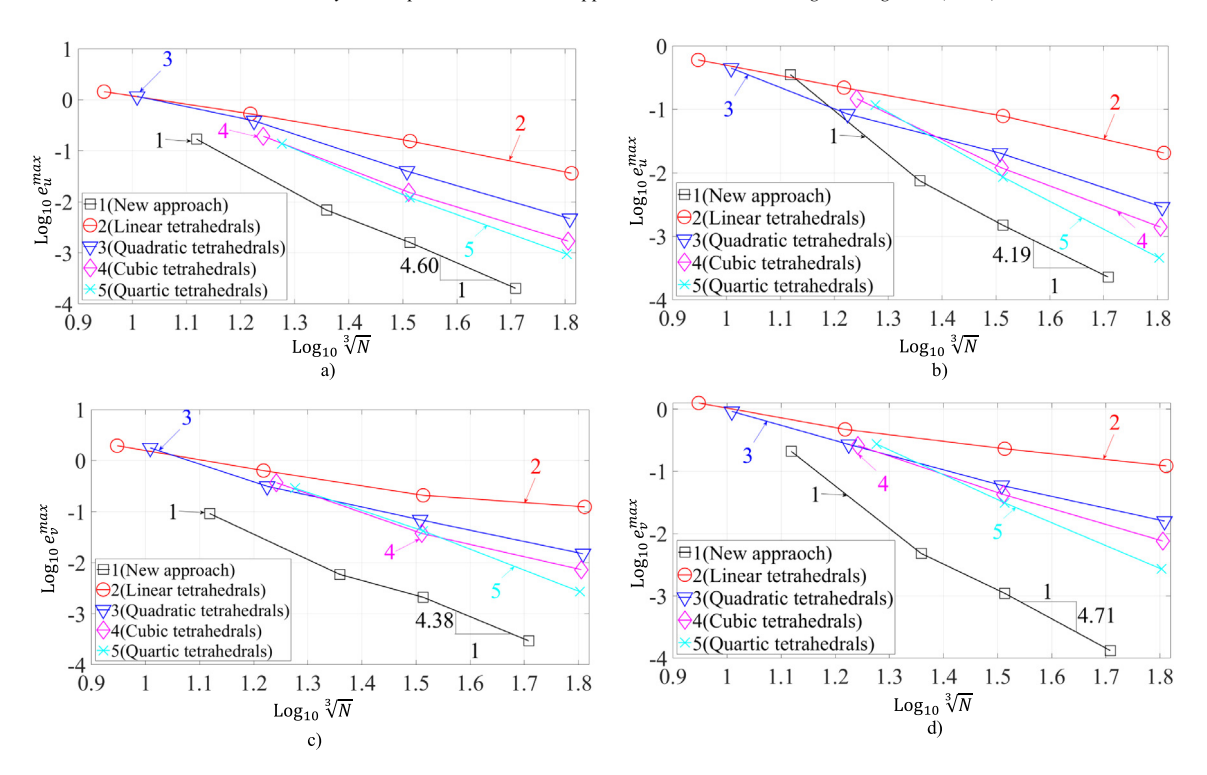


Fig. 7. The maximum relative errors in displacement  $e_u^{max}$  (a, b) and in velocity  $e_v^{max}$  (c, d) as a function of  $\sqrt[3]{N}$  in the logarithmic scale at mesh refinement. N is the number of degrees of freedom. The numerical solutions of the 3-D wave equation with zero (a, c) and non-zero (b, d) loading functions for the prism with the spherical hole (see Fig. 5a) are obtained by the new approach on cubic ( $b_y = b_z = 1$ ) Cartesian meshes (curve 1) and by the tetrahedral linear (curve 2), quadratic (curve 3), cubic (curve 4) and quartic (curve 5) finite elements. Symbols  $\Box$ ,  $\bigcirc$ ,  $\bigtriangledown$ ,  $\diamond$  and  $\times$  correspond to the results for the different N used in the calculations.

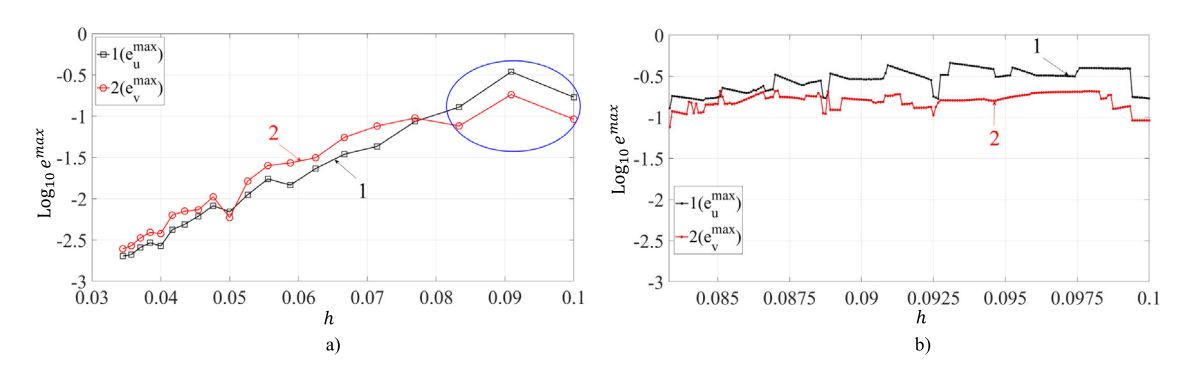


Fig. 8. The maximum relative errors in displacement  $e_u^{max}$  (curve 1) and in velocity  $e_v^{max}$  (curve 2) as a function of mesh size h in the logarithmic scale at mesh refinement for the prism with the spherical hole (see Fig. 5a). The numerical solutions of the 3-D wave equation with zero loading function are obtained by the new approach on cubic ( $b_y = b_z = 1$ ) Cartesian meshes. (b) zooms (a) in the interval  $0.083 \le h \le 0.1$ . Symbols  $\square$  and  $\bigcirc$  correspond to the results for the different h used in the calculations.

seen from Fig. 8a, at small variations of the grid size h the new approach converges with small oscillations. The magnitudes of these oscillations become smaller with the decrease in h. One of the oscillations in Fig. 8a between the mesh sizes  $h_1 \approx 0.083$  and  $h_2 = 0.1$  is shown in Fig. 8b in more detail using smaller increments  $\Delta h = \frac{h_2 - h_1}{200}$  (for the selected meshes point A in 5a always coincides with a grid point whereas point B is located between grid points of Cartesian meshes). Now much more oscillations can be observed between the mesh sizes  $h_1 \approx 0.083$  and  $h_2 = 0.1$ . The oscillations of the curves in Fig. 8b are explained by the following two facts: a) the complicated dependence of the leading terms of the local truncation error on the coefficients  $d_i$  that define the location of the grid

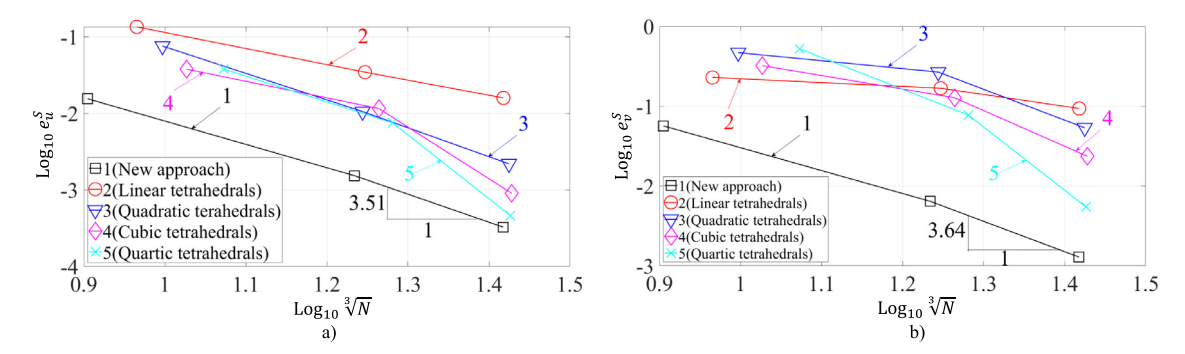


Fig. 9. The relative errors in displacement  $e_u^S$  (a) and in velocity  $e_v^S$  (b) at point S(0.2, 0.2, 0.4) as a function of  $\sqrt[3]{N}$  in the logarithmic scale at mesh refinement. N is the number of degrees of freedom. The numerical solutions of the 3-D wave equation for the prism with the spherical hole (see Fig. 5a) are obtained by the new approach on cubic  $(b_y = b_z = 1)$  Cartesian meshes (curve 1) and by the tetrahedral linear (curve 2), quadratic (curve 3), cubic (curve 4) and quartic (curve 5) finite elements. Symbols  $\square$ ,  $\bigcirc$ ,  $\triangledown$ ,  $\diamond$  and  $\times$  correspond to the results for the different N used in the calculations.

points in the non-uniform stencil; and b) small jumps in curves 1 and 2 in Fig. 8b are related to the discontinuous change in the location of the grid points with respect to the boundary (e.g., some grid points that are located close the boundary inside the domain or are located on the boundary for one mesh size h will be located outside the domain at very small variation of the grid size  $\Delta h$ ). It is important to mention that these oscillations in accuracy at the variation of the mesh size h are typical for numerical techniques on irregular domains. For example, at the transition from one finite element mesh to another one with approximately the same element sizes, the finite changes in the angles of finite elements can occur. This also leads to the oscillations in the convergence of the finite element techniques. We should also mention that the detailed study of convergence of the new approach (similar to that in Fig. 8) was conducted for all numerical examples considered in this paper and it showed that the new approach yields stable and convergence results.

# 4.1.3. A prism with a spherical hole (with a reference solution)

In this Section we solve a test problem for the prism with the spherical hole (see Fig. 5a) with the Neumann and Dirichlet boundary conditions described by different functions. The initial, boundary conditions and the loading term for the 3-D wave equation are given as follows: the initial displacements and velocities over the entire domain  $u(x, y, z, t = 0) = \cos(10x+7y+5z)$  and v(x, y, z, t = 0) = 0; the Neumann boundary conditions  $g_1(x, y, z, t) = 0$  on the face OPQR and  $g_2(x, y, z, t) = (x^2 + y^2 + z^2)\cos(3\pi t)$  on the spherical hole; the Dirichlet boundary conditions  $g_3(y, z, t) = \cos(7y + 5z)\cos(10t)$  on the face ADOP,  $g_4(x, z, t) = \cos(10x + 5z)\cos(10t)$  on the face ABQP,  $g_5(x, y, t) = \cos(10x + 7y)\cos(10t)$  on the face ABCD,  $g_6(x, z, t) = \cos(10x + 5z + 7)\cos(10t)$  on the face CDOR,  $g_7(y, z, t) = \cos(10 + 7y + 5z)\cos(10t)$  on the face BCRQ; and non-zero load f(x, y, z, t) = 10. The wave velocity c = 1 and the observation time c = 0.2 are selected. For this problem the exact solution is unknown. Therefore, the numerical solution obtained on a fine mesh with the c = 0.2 the errors.

In order to estimate the order of convergence of the new approach and to compare the accuracy of the numerical solutions obtained by different techniques we select a point S inside the domain with the coordinates (0.2, 0.2, 0.4) and plot the errors in displacement  $e_u^S$  and in velocity  $e_v^S$  at this point S; see Fig. 9 with the errors plotted in the logarithmic scale at mesh refinement. Fig. 9 shows that at the same number N of degrees of freedom the results obtained by the new approach are more accurate than those obtained by the conventional linear and high-order (up to the fourth order) finite elements (similar results can be obtained at other points). It can be also seen from Fig. 9 that the order of convergence of the new approach for the displacement and velocity exceeds three.

It can be concluded that for the 3-D wave equation with the Neumann and Dirichlet boundary conditions on irregular domains, the new approach with the 27-point stencils (similar to those for the linear quadrilateral finite elements) yields much more accurate numerical results than those obtained by the linear and high-order (up to the fourth order) finite elements at the same number of degrees of freedom. Moreover, higher order finite elements require much more computation time due to much wider stencil equations compared to those for the new approach.

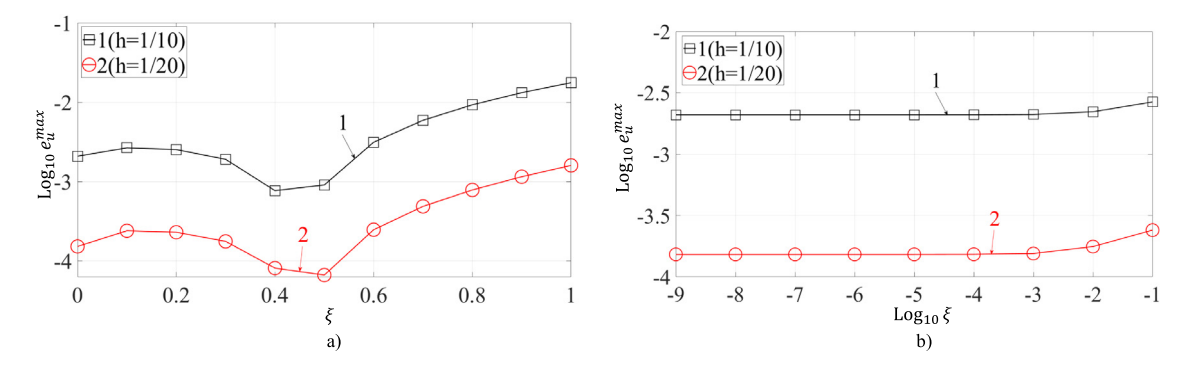


Fig. 10. The logarithm of the maximum relative error in temperature  $e_u^{max}$  as a function of the coefficient  $\xi$  (a) and  $\log_{10}\xi$  (b) at small  $\xi$ . The numerical solutions of the 3-*D* heat equation with zero source for the rectangular parallelepiped (see Fig. 3) are obtained by the new approach on cubic ( $b_y = b_z = 1$ ) Cartesian meshes of sizes h = 1/10 (curve 1) and h = 1/20 (curve 2). (b) zoom (a) along the *x*-axis at  $0 \le \xi \le 0.1$ . Symbols  $\square$  and  $\square$  correspond to the results for the different coefficients  $\xi$  used in the calculations.

# 4.2. 3-D heat equation

Here, we consider two test problems for the heat equation on regular and irregular domains with the following exact solutions:

$$u(x, y, z, t) = \eta_1 e^{\beta_1(x-1) + \beta_2(y-1) - a\beta_4 t} \sin(\beta_3 z)$$
(38)

with  $\eta_1 = 50$ ,  $\beta_1 = 4$ ,  $\beta_2 = 12$ ,  $\beta_3 = 4\pi$ ,  $\beta_4 = (\beta_3^2 - \beta_1^2 - \beta_2^2)$  and zero loading function f = 0, and

$$u(x, y, z, t) = \eta_2 \sin(\beta_5 x) \cos(\beta_6 y) \sin(\beta_7 z) e^{(\beta_8 t)}$$
(39)

with  $\eta_2 = 200$ ,  $\beta_5 = 5\pi$ ,  $\beta_6 = 4\pi$ ,  $\beta_7 = 3\pi$ ,  $\beta_8 = -2\pi$  and non-zero source  $f(x, y, z, t) = \eta_2(\beta_8 + a(\beta_5^2 + \beta_6^2 + \beta_7^2))\sin(\beta_5 x)\cos(\beta_6 y)\sin(\beta_7 z)e^{(\beta_8 t)}$ . The thermal diffusivity a = 100 and the observation times T = 0.002 (due to the selected exponential solution in time, Eq. (38), there is a significant change in temperature during this time) for zero source and T = 0.2 for non-zero source are selected. For these problems, the initial and boundary conditions are applied according to the exact solutions, Eqs. (38) and (39).

# 4.2.1. A rectangular parallelepiped

Similar to the wave equation, first let us analyze the effect of matched and non-matched cubic ( $b_y = b_z = 1$ ) Cartesian meshes on the accuracy of the numerical solutions obtained by the new approach for the rectangular parallelepiped ABCDOPQR (see Fig. 3) with the exact solution given by Eq. (38). The Dirichlet boundary conditions are imposed on all faces except the face OPQR where the Neumann boundary conditions are imposed. The non-matched meshes with the 27-points non-uniform and uniform stencils are formed similar to those in Section 4.1.1.

Fig. 10 shows the logarithm of the maximum relative error in temperature  $e_u^{max}$  as a function of  $\xi$  at the selected mesh sizes h=1/10 and h=1/20. As can be seen from Fig. 10, the error  $e_u^{max}$  is practically constant at very small  $\xi$  ( $10^{-9} \le \xi \le 10^{-3}$ ) and slightly varies at small  $\xi$  ( $10^{-3} \le \xi \le 0.3$ ). Moreover, at these small  $\xi$  ( $10^{-9} \le \xi \le 0.3$ ), the error  $e_u^{max}$  is smaller than that at  $\xi=1$  corresponding to the matched meshes. This means that the large differences in distances between the points included into the non-uniform stencil do not worsen the accuracy of the new approach.

## 4.2.2. A prism with a spherical hole

Next, let us analyze the application of the new approach to the 3-D heat equation with zero and non-zero sources on a more complex irregular domain represented by the prism ABCDOPQR with the spherical hole; see Fig. 5a. Two problems for the 3-D heat equation with zero and non-zero sources are solved by the new approach on the irregular domain. The Neumann boundary conditions are imposed on the upper face ROPQ and on the spherical surface of the hole whereas the Dirichlet boundary conditions are imposed on all other faces; see Fig. 5a. An example of a cubic  $(b_y = b_z = 1)$  Cartesian mesh used with the new approach is shown in Fig. 5b.

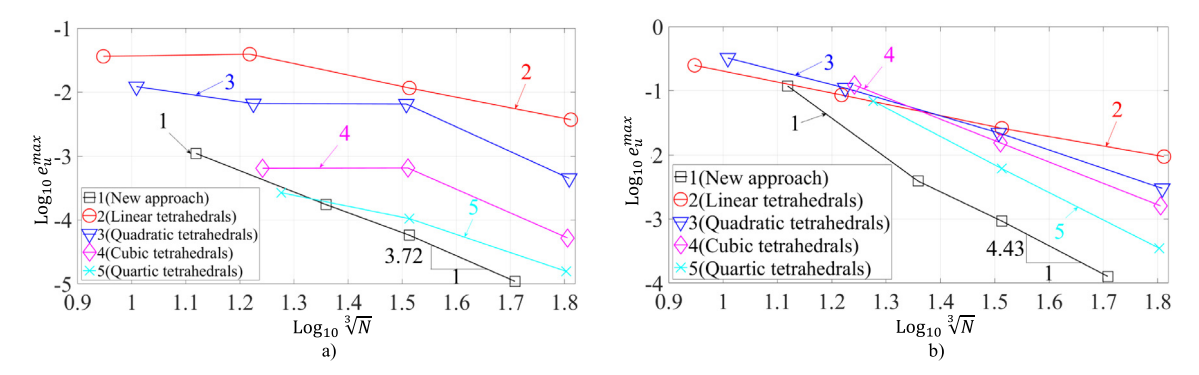


Fig. 11. The maximum relative error in temperature  $e_u^{max}$  as a function of  $\sqrt[3]{N}$  in the logarithmic scale at mesh refinement. N is the number of degrees of freedom. The numerical solutions of the 3-D heat equation with zero (a) and non-zero (b) sources for the prism with the spherical hole (see Fig. 5a) are obtained by the new approach on cubic ( $b_y = b_z = 1$ ) Cartesian meshes (curve 1) and by the tetrahedral linear (curve 2), quadratic (curve 3), cubic (curve 4) and quartic (curve 5) finite elements. Symbols  $\Box$ ,  $\bigcirc$ ,  $\bigtriangledown$ ,  $\diamond$  and  $\times$  correspond to the results for the different N used in the calculations.

Fig. 11 presents the error  $e_u^{max}$  as a function of the number of degrees of freedom N in the logarithmic scale obtained by the new approach (curves 1) and by the conventional finite elements (curves 2–5) at mesh refinement. As stated earlier the slopes of curves 1 at large N in Fig. 11 approximately describe the order of accuracy of the new approach because  $\sqrt[3]{N}$  is approximately proportional to the mesh size h. It can be seen from Fig. 11 that the order of accuracy of the new approach exceeds three for the temperature. This is in agreement with the theoretical results in Section 2.

Curves 2–5 in Fig. 11 present the error  $e_u^{max}$  for the tetrahedral linear and high-order finite elements (see Fig. 6 for an example of a tetrahedral finite element mesh for the prism with the spherical hole). It can be seen from Fig. 11 that at the same N the new approach yields more accurate results than those obtained by the conventional linear and high-order (up to the fourth order) finite elements. It is important to mention that the high-order finite elements have much wider stencils and require much more computation time compared to that for the new approach at the same N.

#### 4.3. 3-D Poisson equation

Here, first we consider two test problems for the Poisson equation on regular and irregular domains with the following exact solutions:

$$u(x, y, z) = \eta e^{\beta_1(x-1) + \beta_2(y-1)} \sin(\beta_3 z)$$
(40)

with  $\beta_1 = 8$ ,  $\beta_2 = \sqrt{(4\pi)^2 - 8^2}$ ,  $\beta_3 = 4\pi$  and zero source f = 0, and

$$u(x, y, z) = \eta \sin(\beta_4 x) \sin(\beta_5 y) \cos(\beta_6 z) \tag{41}$$

with  $\beta_4 = 5\pi$ ,  $\beta_5 = 4\pi$ ,  $\beta_6 = 3\pi$  and non-zero source  $f(x, y, z) = -\eta(\beta_4^2 + \beta_5^2 + \beta_6^2)\sin(\beta_4 x)\sin(\beta_5 y)\cos(\beta_6 z)$ . In Eqs. (40) and (41) the coefficient  $\eta = 100$  is used. For these problems, the combined Neumann and Dirichlet boundary conditions are applied according to the exact solutions, Eqs. (40) and (41).

### 4.3.1. A rectangular parallelepiped

Similar to the wave and heat equations, first let us analyze the effect of matched and non-matched cubic  $(b_y = b_z = 1)$  Cartesian meshes on the accuracy of the numerical solutions obtained by the new approach for the rectangular parallelepiped ABCDOPQR (see Fig. 3) with the exact solution given by Eq. (40). The Dirichlet boundary conditions are imposed on all faces except the face OPQR where the Neumann boundary conditions are imposed. The non-matched meshes with the 27-points non-uniform and uniform stencils are formed similar to those in Section 4.1.1.

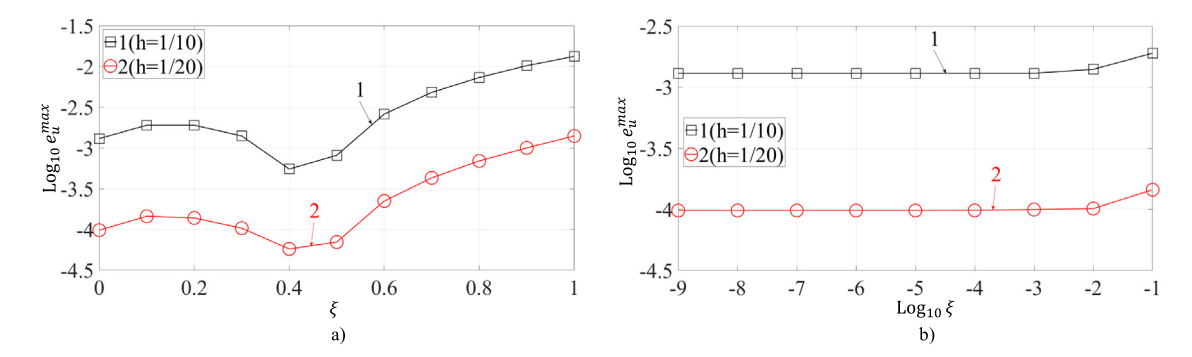


Fig. 12. The logarithm of the maximum relative error in temperature  $e_u^{max}$  as a function of the coefficient  $\xi$  (a) and  $\log_{10}\xi$  (b) at small  $\xi$ . The numerical solutions of the 3-D Poisson equation with zero source for the rectangular parallelepiped (see Fig. 3) are obtained by the new approach on cubic ( $b_y = b_z = 1$ ) Cartesian meshes of sizes h = 1/10 (curve 1) and h = 1/20 (curve 2). (b) zoom (a) along the x-axis at  $0 \le \xi \le 0.1$ . Symbols  $\square$  and  $\bigcirc$  correspond to the results for the different coefficients  $\xi$  used in the calculations.

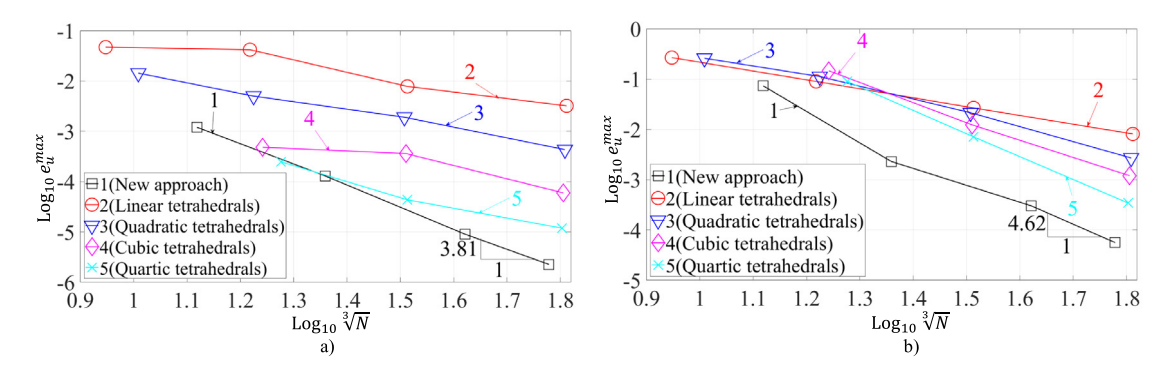


Fig. 13. The maximum relative error in temperature  $e_u^{max}$  as a function of  $\sqrt[3]{N}$  in the logarithmic scale at mesh refinement. N is the number of degrees of freedom. The numerical solutions of the 3-D Poisson equation with zero (a) and non-zero (b) sources for the prism with the spherical hole (see Fig. 5a) are obtained by the new approach on cubic  $(b_y = b_z = 1)$  Cartesian meshes (curve 1) and by the tetrahedral linear (curve 2), quadratic (curve 3), cubic (curve 4) and quartic (curve 5) finite elements. Symbols  $\Box$ ,  $\bigcirc$ ,  $\bigtriangledown$ ,  $\diamond$  and  $\times$  correspond to the results for the different N used in the calculations.

Fig. 12 shows the logarithm of the maximum relative error in temperature  $e_u^{max}$  as a function of  $\xi$  at the selected mesh sizes h=1/10 and h=1/20. As can be seen from Fig. 12, the error  $e_u^{max}$  is practically constant at very small  $\xi$  ( $10^{-9} \le \xi \le 10^{-3}$ ) and slightly varies at small  $\xi$  ( $10^{-3} \le \xi \le 0.3$ ). Moreover, at these small  $\xi$  ( $10^{-9} \le \xi \le 0.3$ ), the error  $e_u^{max}$  is smaller than that at  $\xi=1$  corresponding to the matched meshes. This means that the large differences in distances between the points included into the non-uniform stencil do not worsen the accuracy of the new approach.

# 4.3.2. A prism with a spherical hole (with the exact solutions given by Eqs. (40) and (41))

Next, let us analyze the application of the new approach to the 3-D Poisson equation with zero and non-zero sources on a more complex irregular domain represented by the prism ABCDOPQR with the spherical hole; see Fig. 5a. Two problems for the 3-D Poisson equation with zero and non-zero sources are solved by the new approach on the irregular domain. The Neumann boundary conditions are imposed on the upper face ROPQ and on the spherical surface of the hole whereas the Dirichlet boundary conditions are imposed on all other faces; see Fig. 5a. An example of a cubic  $(b_v = b_z = 1)$  Cartesian mesh used with the new approach is shown in Fig. 5b.

Fig. 13 presents the error  $e_u^{max}$  as a function of the number of degrees of freedom N in the logarithmic scale obtained by the new approach (curves 1) and by the conventional finite elements (curves 2–5) at mesh refinement. As stated earlier the slopes of curves 1 at large N in Fig. 13 approximately describe the order of accuracy of the new approach because  $\sqrt[3]{N}$  is approximately proportional to the mesh size h. It can be seen from Fig. 13 that the

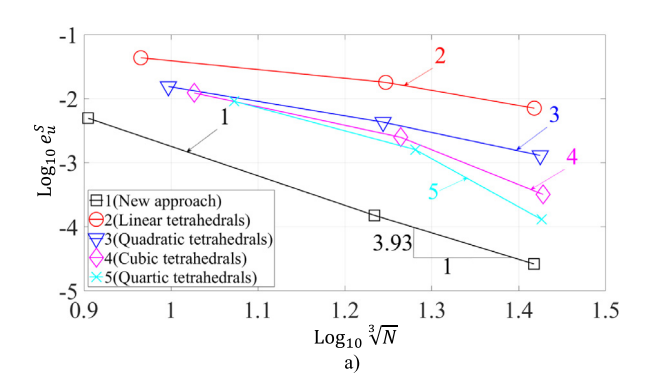


Fig. 14. The relative error in temperature  $e_u^S$  at point S(0.2, 0.2, 0.4) as a function of  $\sqrt[3]{N}$  in the logarithmic scale at mesh refinement. N is the number of degrees of freedom. The numerical solutions of the 3-D Poisson equation for the prism with the spherical hole (see Fig. 5a) are obtained by the new approach on cubic  $(b_y = b_z = 1)$  Cartesian meshes (curve 1) and by the tetrahedral linear (curve 2), quadratic (curve 3), cubic (curve 4) and quartic (curve 5) finite elements. Symbols  $\Box$ ,  $\bigcirc$ ,  $\bigtriangledown$ ,  $\diamond$  and  $\times$  correspond to the results for the different N used in the calculations.

order of accuracy of the new approach exceeds three for the temperature. This is in agreement with the theoretical results in Section 3.

Curves 2–5 in Fig. 13 present the error  $e_u^{max}$  for the tetrahedral linear and high-order finite elements (see Fig. 6 for an example of a tetrahedral finite element mesh for the prism with the spherical hole). It can be seen from Fig. 13 that at the same N the new approach yields more accurate results than those obtained by the conventional linear and high-order (up to the fourth order) finite elements. It is important to mention that the high-order finite elements have much wider stencils and require much more computation time compared to that for the new approach at the same N.

#### 4.3.3. A prism with a spherical hole (with a reference solution)

Here, we solve a test problem for the prism with the spherical hole (see Fig. 5a) with the Neumann and Dirichlet boundary conditions described by different functions. The boundary conditions and the source term for the 3-D Poisson equation are given as follows: the Neumann boundary conditions  $g_1(x, y, z) = x^2y^3e^{10(z-1)}$  on the face OPQR and  $g_2(x, y, z) = \sin(7x - 5y + 2z)$  on the spherical hole; the Dirichlet boundary conditions  $g_3(y, z) = \cos(3\pi(4z-3y))$  on the face ADOP,  $g_4(x, z) = \cos(2\pi(5x+6z))$  on the face ABQP,  $g_5(x, y) = \cos(\pi(10x-9y))$  on the face ABCD,  $g_6(x, z) = -\cos(2\pi(5x+6z))$  on the face CDOR,  $g_7(y, z) = \cos(3\pi(4z-3y))$ ) on the face BCRQ; and the non-zero source  $f(x, y, z) = 50(x^2 + y^2 + z^2)$ . For this problem the exact solution is unknown. Therefore, the numerical solution obtained on a fine mesh with the 7th order finite elements and with 1, 352, 444 degrees of freedom is selected as the reference solution for the calculation of the errors.

Similar to Section 4.1.3, in order to estimate the order of convergence of the new approach and to compare the accuracy of the numerical solutions obtained by different techniques we select a point S inside the domain with the coordinates (0.2, 0.2, 0.4) and plot the error in temperature  $e_u^S$  at this point S; see Fig. 14 with the errors plotted in the logarithmic scale at mesh refinement. Fig. 14 shows that at the same number N of degrees of freedom the results obtained by the new approach are more accurate than those obtained by the conventional linear and high-order (up to the fourth order) finite elements (similar results can be obtained at other points). It can be also seen from Fig. 9 that the order of convergence of the new approach exceeds three.

It can be concluded that for the 3-D Poisson equation with the Neumann and Dirichlet boundary conditions on irregular domains, the new approach with the 27-point stencils (similar to those for the linear quadrilateral finite elements) yields much more accurate numerical results than those obtained by the linear and high-order (up to the fourth order) finite elements at the same number of degrees of freedom. Moreover, higher order finite elements require much more computation time due to much wider stencil equations compared to those for the new approach.

# 5. Concluding remarks

A new 3-D numerical approach has been developed and applied to a number of partial differential equations on irregular domains with the Neumann and Dirichlet boundary conditions. It is based on the 27-point uniform and

non-uniform stencils that are similar to those for the linear quadrilateral finite elements. The main advantages of the suggested technique can be summarized as follows:

- Many difficulties of the existing numerical techniques for irregular domains (e.g., the finite elements, spectral element, isogeometric elements, the finite volume method, and many other) especially in the 3-D case are related to complicated mesh generators and the accuracy of 'bad' elements (e.g., the elements with small angles). In contrast to these techniques, the new approach is based on trivial Cartesian meshes with a simple procedure for the formation of the 27-point nonuniform stencils for the grid points located close to the boundary. Moreover, very small distances  $(0.1h 10^{-9}h)$  where h is the grid size) between the grid points of a Cartesian mesh and the boundary (i.e., some coefficients  $d_i$  of the non-uniform stencil are close to zero while some other coefficients  $d_i$  of the same stencil equal unity; see Fig. 2) do not worsen the accuracy of the new technique.
- In contrast to the finite-difference techniques with the stencil coefficients calculated through the approximation of separate partial derivatives, the entire partial differential equation is used for the calculation of the stencil coefficients in the new approach. This leads to the optimal accuracy of the proposed technique. E.g., the 27-point uniform and nonuniform stencils of the new approach provide the optimal accuracy that cannot be improved without changing the width of stencil equations. In contrast to the 27-point stencils of the linear quadrilateral finite elements, the new approach yields a much higher order of accuracy.
- One of the important features of the new approach with the Neumann boundary conditions is the formation of the final semi-discrete system of equations without including the unknowns at the boundary; i.e., all unknowns are introduced at the internal grid points and the Neumann boundary conditions are used as the known right-hand side for the final system of equations. This feature is promising for the application of the new approach to the problems with moving boundaries (e.g., crack propagation) because there is no need to redefine meshes for moving boundaries as in many existing approaches (e.g., FEM). The application of the new approach to such problems will be considered in the future.
- The numerical results for irregular domains also show that at the same number of degrees of freedom, the new approach is even much more accurate than the high-order (up to the fourth order) tetrahedral finite elements with much wider stencils. This also means that at a given accuracy, the new approach significantly reduces the computation time compared to the linear and high-order finite elements.
- The new approach does not require time consuming numerical integration for finding the coefficients of the stencil equations; e.g., as for the high-order finite, spectral and isogeometric elements. For the new technique, the coefficients of the uniform stencils for the grid points located far from the boundary are calculated analytically. For the grid points located close to the boundary, the coefficients of the nonuniform stencils are calculated numerically by the solution of small local systems of linear algebraic equations. Numerical experiments show that the solution of these small local systems of algebraic equations is fast. Moreover, these local systems are independent of each other and can be efficiently solved on a parallel computer.
- It has been shown that the wave and heat equations can be uniformly treated with the new approach. The order of the time derivative in these equations does not affect the coefficients of the stencil equations of the semi-discrete systems because in the presented derivations the space discretization is considered independent of the time discretization without the interaction between the errors in space and time.

It is interesting to note that the final formulas for the calculation of the stencil coefficients do not include the derivatives of the solution and the new approach can be also applied to the problems with reduced regularity (smoothness). In our paper [30] the 1-D impact wave propagation problem with a propagating discontinuity has been solved by the new approach on matched and non-matched meshes as well as by the conventional finite elements. The numerical results in [30] show that even in this case the new approach yields more accurate results compared to those obtained by the conventional finite elements. We observed similar effects for the isogeometric elements applied to the same 1-D impact problem; i.e., the approximation of discontinuous solutions by smooth functions of high-order isogeometric elements yields accurate results.

In the future we plan to consider the stencils with a larger number of grid points for a higher order of accuracy (similar to the high-order finite elements or to the high-order finite-difference techniques), to consider a mesh refinement with uniform Cartesian meshes using special stencils for the transition from a fine mesh to a coarse mesh,

to apply the proposed technique to the wave and heat equations with variable and piecewise-constant coefficients as well as to other partial differential equations, to solve real-world problems with the new approach.

# Acknowledgments

The research has been supported in part by the Air Force Office of Scientific Research, United States (contract FA9550-16-1-0177), by the National Science Foundation, United States grant CMMI-1935452 and by Texas Tech University, United States.

# Appendix A. The coefficients $b_p$ used in Eq. (15)

The first five coefficients  $b_i$  (i = 1, 2, ..., 5) are presented below. All coefficients  $b_i$  (i = 1, 2, ..., 165) used in the paper are given in the attached file 'b-coeff-wave.pdf'

 $b_1 = k_1 + k_{10} + k_{11} + k_{12} + k_{13} + k_{14} + k_{15} + k_{16} + k_{17} + k_{18} + k_{19} + k_2 + k_{20} + k_{21} + k_{22} + k_{23} + k_{24} + k_{25} + k_{26} + k_{27} + k_3 + k_4 + k_5 + k_6 + k_7 + k_8 + k_9$ 

 $b_2 = -d_1k_1 - d_{10}k_{10} + d_{12}k_{12} - d_{13}k_{13} + d_{15}k_{15} - d_{16}k_{16} + d_{18}k_{18} - d_{19}k_{19} + d_{21}k_{21} - d_{22}k_{22} + d_{24}k_{24} - d_{25}k_{25} + d_{27}k_{27} + d_3k_3 - d_4k_4 + d_6k_6 - d_7k_7 + d_9k_9 + \bar{k}_1n_{1,1} + \bar{k}_{10}n_{1,10} + \bar{k}_{11}n_{1,11} + \bar{k}_{12}n_{1,12} + \bar{k}_{13}n_{1,13} + \bar{k}_{14} + \bar{k}_{15}n_{1,15} + \bar{k}_{16}n_{1,16} + \bar{k}_{17}n_{1,17} + \bar{k}_{18}n_{1,18} + \bar{k}_{19}n_{1,19} + \bar{k}_2n_{1,2} + \bar{k}_2n_{1,20} + \bar{k}_{21}n_{1,21} + \bar{k}_{22}n_{1,22} + \bar{k}_{23}n_{1,23} + \bar{k}_{24}n_{1,24} + \bar{k}_{25}n_{1,25} + \bar{k}_{26}n_{1,26} + \bar{k}_{27}n_{1,27} + \bar{k}_3n_{1,3} + \bar{k}_4n_{1,4} + \bar{k}_5n_{1,5} + \bar{k}_6n_{1,6} + \bar{k}_7n_{1,7} + \bar{k}_8n_{1,8} + \bar{k}_9n_{1,9}$ 

 $b_3 = b_y (-d_1k_1 - d_{10}k_{10} - d_{11}k_{11} - d_{12}k_{12} + d_{16}k_{16} + d_{17}k_{17} + d_{18}k_{18} - d_{19}k_{19} - d_2k_2 - d_{20}k_{20} - d_{21}k_{21} + d_{25}k_{25} + d_{26}k_{26} + d_{27}k_{27} - d_3k_3 + d_7k_7 + d_8k_8 + d_9k_9) + \bar{k}_1n_{2,1} + \bar{k}_{10}n_{2,10} + \bar{k}_{11}n_{2,11} + \bar{k}_{12}n_{2,12} + \bar{k}_{13}n_{2,13} + \bar{k}_{14} + \bar{k}_{15}n_{2,15} + \bar{k}_{16}n_{2,16} + \bar{k}_{17}n_{2,17} + \bar{k}_{18}n_{2,18} + \bar{k}_{19}n_{2,19} + \bar{k}_{2}n_{2,2} + \bar{k}_{20}n_{2,20} + \bar{k}_{21}n_{2,21} + \bar{k}_{22}n_{2,22} + \bar{k}_{23}n_{2,23} + \bar{k}_{24}n_{2,24} + \bar{k}_{25}n_{2,25} + \bar{k}_{26}n_{2,26} + \bar{k}_{27}n_{2,27} + \bar{k}_{3}n_{2,3} + \bar{k}_{4}n_{2,4} + \bar{k}_{5}n_{2,5} + \bar{k}_{6}n_{2,6} + \bar{k}_{7}n_{2,7} + \bar{k}_{8}n_{2,8} + \bar{k}_{9}n_{2,9}$ 

 $b_4 = b_z(-d_1k_1 + d_19k_{19} - d_2k_2 + d_{20}k_{20} + d_{21}k_{21} + d_{22}k_{22} + d_{23}k_{23} + d_{24}k_{24} + d_{25}k_{25} + d_{26}k_{26} + d_{27}k_{27} - d_3k_3 - d_4k_4 - d_5k_5 - d_6k_6 - d_7k_7 - d_8k_8 - d_9k_9) + \bar{k}_1n_{3,1} + \bar{k}_{10}n_{3,10} + \bar{k}_{11}n_{3,11} + \bar{k}_{12}n_{3,12} + \bar{k}_{13}n_{3,13} + \bar{k}_{14} + \bar{k}_{15}n_{3,15} + \bar{k}_{16}n_{3,16} + \bar{k}_{17}n_{3,17} + \bar{k}_{18}n_{3,18} + \bar{k}_{19}n_{3,19} + \bar{k}_{2}n_{3,2} + \bar{k}_{20}n_{3,20} + \bar{k}_{21}n_{3,21} + \bar{k}_{22}n_{3,22} + \bar{k}_{23}n_{3,23} + \bar{k}_{24}n_{3,24} + \bar{k}_{25}n_{3,25} + \bar{k}_{26}n_{3,26} + \bar{k}_{27}n_{3,27} + \bar{k}_3n_{3,3} + \bar{k}_4n_{3,4} + \bar{k}_5n_{3,5} + \bar{k}_6n_{3,6} + \bar{k}_7n_{3,7} + \bar{k}_8n_{3,8} + \bar{k}_9n_{3,9}$ 

 $b_5 = \frac{1}{2}(2m_1 + 2m_{10} + 2m_{11} + 2m_{12} + 2m_{13} + 2m_{14} + 2m_{15} + 2m_{16} + 2m_{17} + 2m_{18} + 2m_{19} + 2m_{2} + 2m_{20} + 2m_{21} + 2m_{22} + 2m_{23} + 2m_{24} + 2m_{25} + 2m_{26} + 2m_{27} + 2m_{3} + 2m_{4} + 2m_{5} + 2m_{6} + 2m_{7} + 2m_{8} + 2m_{9} + d_{1}^{2}k_{1} - 2d_{1}\bar{k}_{1}n_{1,1} + d_{10}^{2}k_{10} - 2d_{10}\bar{k}_{10}n_{1,10} + d_{12}^{2}k_{12} + 2d_{12}\bar{k}_{12}n_{1,12} + d_{13}^{2}k_{13} - 2d_{13}\bar{k}_{13}n_{1,13} + d_{15}^{2}k_{15} + 2d_{15}\bar{k}_{15}n_{1,15} + d_{16}^{2}k_{16} - 2d_{16}\bar{k}_{16}n_{1,16} + d_{18}^{2}k_{18} + 2d_{18}\bar{k}_{18}n_{1,18} + d_{19}^{2}k_{19} - 2d_{19}\bar{k}_{19}n_{1,19} + d_{21}^{2}k_{21} + 2d_{21}\bar{k}_{21}n_{1,21} + d_{22}^{2}k_{22} - 2d_{22}\bar{k}_{22}n_{1,22} + d_{24}^{2}k_{24} + 2d_{24}\bar{k}_{24}n_{1,24} + d_{25}^{2}k_{25} - 2d_{25}\bar{k}_{25}n_{1,25} + d_{27}^{2}k_{27} + 2d_{27}\bar{k}_{27}n_{1,27} + d_{3}^{2}k_{3} + 2d_{3}\bar{k}_{3}n_{1,3} + d_{4}^{2}k_{4} - 2d_{4}\bar{k}_{4}n_{1,4} + d_{6}^{2}k_{6} + 2d_{6}\bar{k}_{6}n_{1,6} + d_{7}^{2}k_{7} - 2d_{7}\bar{k}_{7}n_{1,7} + d_{9}^{2}k_{9} + 2d_{9}\bar{k}_{9}n_{1,9})$ 

# Appendix B. The explicit expression for the term $\bar{f}_{14}$ in Eq. (24) in the case of nonzero load (source) $f \neq 0$ in the wave (heat) equation

The expression for  $\bar{f}_{14}$  including the first two orders with respect to  $\boldsymbol{h}$  is presented below. The expression for  $\bar{f}_{14}$  up to the eight order with respect to  $\boldsymbol{h}$  is given in the attached file 'RHS-wave.pdf'

$$\begin{split} &\bar{f}_{14} = \mathbf{h}^2(m_1 + m_{10} + m_{11} + m_{12} + m_{13} + m_{14} + m_{15} + m_{16} + m_{17} + m_{18} + m_{19} + m_2 + m_{20} + m_{21} + m_{22} + m_{23} + m_{24} + m_{25} + m_{26} + m_{27} + m_3 + m_4 + m_5 + m_6 + m_7 + m_8 + m_9) f_{14} \\ &+ \mathbf{h}^3((b_z(-d_1m_1 + d_19m_{19} - d_2m_2 + d_{20}m_{20} + d_{21}m_{21} + d_{22}m_{22} + d_{23}m_{23} + d_{24}m_{24} + d_{25}m_{25} + d_{26}m_{26} + d_{27}m_{27} - d_3m_3 - d_4m_4 - d_5m_5 - d_6m_6 - d_7m_7 - d_8m_8 - d_9m_9) + \bar{m}_{14} + \bar{m}_{10}n_{3,10} + \bar{m}_{11}n_{3,11} + \bar{m}_{12}n_{3,12} + \bar{m}_{13}n_{3,13} + \bar{m}_{15}n_{3,15} + m_{16}n_{3,16} + \bar{m}_{17}n_{3,17} + \bar{m}_{18}n_{3,18} + \bar{m}_{19}n_{3,19} + \bar{m}_{2}n_{3,2} + \bar{m}_{20}n_{3,20} + \bar{m}_{21}n_{3,21} + \bar{m}_{22}n_{3,22} + \bar{m}_{23}n_{3,23} + \bar{m}_{24}n_{3,24} + \bar{m}_{25}n_{3,25} + \bar{m}_{26}n_{3,26} + \bar{m}_{27}n_{3,27} + \bar{m}_{3}n_{3,3} + \bar{m}_{4}n_{3,4} + \bar{m}_{5}n_{3,5} + \bar{m}_{6}n_{3,6} + \bar{m}_{7}n_{3,7} + \bar{m}_{8}n_{3,8} + \bar{m}_{9}n_{3,9}) f_{14}^{(0,0,1)} + (b_y(-d_1m_1 - d_{10}m_{10} - d_{11}m_{11} - d_{12}m_{12} + d_{16}m_{16} + d_{17}m_{17} + d_{18}m_{18} - d_{19}m_{19} - d_{2}m_{2} - d_{20}m_{20} - d_{21}m_{21} + d_{25}m_{25} + d_{26}m_{26} + d_{27}m_{27} - d_{3}m_3 + d_{7}m_7 + d_{8}m_8 + d_{9}m_9) + \bar{m}_{14} + \bar{m}_{10}n_{2,10} + \bar{m}_{11}n_{2,11} + \bar{m}_{12}n_{2,12} + \bar{m}_{13}n_{2,13} + \bar{m}_{15}n_{2,15} + \bar{m}_{16}n_{2,16} + \bar{m}_{17}n_{2,17} + \bar{m}_{18}n_{2,18} + \bar{m}_{19}n_{2,19} + \bar{m}_{2}n_{2,2} + \bar{m}_{20}n_{2,20} + \bar{m}_{21}n_{2,21} + \bar{m}_{22}n_{2,22} + \bar{m}_{23}n_{2,23} + \bar{m}_{24}n_{2,24} + \bar{m}_{25}n_{2,25} + \bar{m}_{26}n_{2,26} + \bar{m}_{27}n_{2,27} + \bar{m}_{3}n_{2,3} + \bar{m}_{4}n_{2,4} + \bar{m}_{5}n_{2,5} + \bar{m}_{6}n_{2,6} + \bar{m}_{7}n_{2,7} + \bar{m}_{8}n_{2,8} + \bar{m}_{9}n_{2,9}) f_{14}^{(0,1,0)} + (-d_{1}m_{1} - d_{10}m_{10} + d_{12}m_{12} - d_{13}m_{13} + d_{15}m_{1,15} + \bar{m}_{16}n_{1,16} + \bar{m}_{17}n_{1,17} + \bar{m}_{18}n_{1,18} + \bar{m}_{19}n_{1,19} + \bar{m}_{21}n_{1,20} + \bar{m}_{21}n_{1,21} + \bar{m}_{22}n_{1,22} + \bar{m}_{23}n_{1,23} + \bar{m}_{24}n_{1,24} + \bar{m}_{25}n_{1,25} + \bar{m}_{26}n_{$$

# Appendix C. The coefficients $b_p$ used in Eq. (28)

The first five coefficients  $b_i$  (i = 1, 2, ..., 5) are presented below. All coefficients  $b_i$  (i = 1, 2, ..., 36) used in the paper are given in the attached file 'b-coeff-Pois.pdf'

 $b_1 = k_1 + k_{10} + k_{11} + k_{12} + k_{13} + k_{14} + k_{15} + k_{16} + k_{17} + k_{18} + k_{19} + k_2 + k_{20} + k_{21} + k_{22} + k_{23} + k_{24} + k_{25} + k_{26} + k_{27} + k_3 + k_4 + k_5 + k_6 + k_7 + k_8 + k_9$ 

 $b_2 = b_z(-d_1k_1 + d_19k_{19} - d_2k_2 + d_{20}k_{20} + d_{21}k_{21} + d_{22}k_{22} + d_{23}k_{23} + d_{24}k_{24} + d_{25}k_{25} + d_{26}k_{26} + d_{27}k_{27} - d_3k_3 - d_4k_4 - d_5k_5 - d_6k_6 - d_7k_7 - d_8k_8 - d_9k_9) + \bar{k}_1n_{3,1} + \bar{k}_{10}n_{3,10} + \bar{k}_{11}n_{3,11} + \bar{k}_{12}n_{3,12} + \bar{k}_{13}n_{3,13} + \bar{k}_{14} + \bar{k}_{15}n_{3,15} + \bar{k}_{16}n_{3,16} + \bar{k}_{17}n_{3,17} + \bar{k}_{18}n_{3,18} + \bar{k}_{19}n_{3,19} + \bar{k}_{2}n_{3,2} + \bar{k}_{20}n_{3,20} + \bar{k}_{21}n_{3,21} + \bar{k}_{22}n_{3,22} + \bar{k}_{23}n_{3,23} + \bar{k}_{24}n_{3,24} + \bar{k}_{25}n_{3,25} + \bar{k}_{26}n_{3,26} + \bar{k}_{27}n_{3,27} + \bar{k}_{3}n_{3,3} + \bar{k}_{4}n_{3,4} + \bar{k}_{5}n_{3,5} + \bar{k}_{6}n_{3,6} + \bar{k}_{7}n_{3,7} + \bar{k}_{8}n_{3,8} + \bar{k}_{9}n_{3,9}$ 

 $b_3 = b_y(-d_1k_1 - d_{10}k_{10} - d_{11}k_{11} - d_{12}k_{12} + d_{16}k_{16} + d_{17}k_{17} + d_{18}k_{18} - d_{19}k_{19} - d_2k_2 - d_{20}k_{20} - d_{21}k_{21} + d_{25}k_{25} + d_{26}k_{26} + d_{27}k_{27} - d_3k_3 + d_7k_7 + d_8k_8 + d_9k_9) + \bar{k}_1n_{2,1} + \bar{k}_{10}n_{2,10} + \bar{k}_{11}n_{2,11} + \bar{k}_{12}n_{2,12} + \bar{k}_{13}n_{2,13} + \bar{k}_{14} + \bar{k}_{15}n_{2,15} + \bar{k}_{16}n_{2,16} + \bar{k}_{17}n_{2,17} + \bar{k}_{18}n_{2,18} + \bar{k}_{19}n_{2,19} + \bar{k}_{2}n_{2,2} + \bar{k}_{20}n_{2,20} + \bar{k}_{21}n_{2,21} + \bar{k}_{22}n_{2,22} + \bar{k}_{23}n_{2,23} + \bar{k}_{24}n_{2,24} + \bar{k}_{25}n_{2,25} + \bar{k}_{26}n_{2,26} + \bar{k}_{27}n_{2,27} + \bar{k}_{3}n_{2,3} + \bar{k}_{4}n_{2,4} + \bar{k}_{5}n_{2,5} + \bar{k}_{6}n_{2,6} + \bar{k}_{7}n_{2,7} + \bar{k}_{8}n_{2,8} + \bar{k}_{9}n_{2,9}$ 

 $b_4 = -d_1k_1 - d_{10}k_{10} + d_{12}k_{12} - d_{13}k_{13} + d_{15}k_{15} - d_{16}k_{16} + d_{18}k_{18} - d_{19}k_{19} + d_{21}k_{21} - d_{22}k_{22} + d_{24}k_{24} - d_{25}k_{25} + d_{27}k_{27} + d_3k_3 - d_4k_4 + d_6k_6 - d_7k_7 + d_9k_9 + \bar{k}_1n_{1,1} + \bar{k}_{10}n_{1,10} + \bar{k}_{11}n_{1,11} + \bar{k}_{12}n_{1,12} + \bar{k}_{13}n_{1,13} + \bar{k}_{14} + \bar{k}_{15}n_{1,15} + \bar{k}_{16}n_{1,16} + \bar{k}_{17}n_{1,17} + \bar{k}_{18}n_{1,18} + \bar{k}_{19}n_{1,19} + \bar{k}_2n_{1,2} + \bar{k}_{20}n_{1,20} + \bar{k}_{21}n_{1,21} + \bar{k}_{22}n_{1,22} + \bar{k}_{23}n_{1,23} + \bar{k}_{24}n_{1,24} + \bar{k}_{25}n_{1,25} + \bar{k}_{26}n_{1,26} + \bar{k}_{27}n_{1,27} + \bar{k}_3n_{1,3} + \bar{k}_4n_{1,4} + \bar{k}_5n_{1,5} + \bar{k}_6n_{1,6} + \bar{k}_7n_{1,7} + \bar{k}_8n_{1,8} + \bar{k}_9n_{1,9}$ 

 $b_5 = \frac{1}{2}((b_z^2-1)d_1^2k_1 + b_z^2d_{19}^2k_{19} + b_z^2d_2^2k_2 + b_z^2d_{20}^2k_{20} + b_z^2d_{21}^2k_{21} + b_z^2d_{22}^2k_{22} + b_z^2d_{23}^2k_{23} + b_z^2d_{24}^2k_{24} + b_z^2d_{25}^2k_{25} + b_z^2d_{26}^2k_{26} + b_z^2d_{27}^2k_{27} + b_z^2d_3^2k_3 + b_z^2d_4^2k_4 + b_z^2d_5^2k_5 + b_z^2d_6^2k_6 + b_z^2d_7^2k_7 + b_z^2d_8^2k_8 + b_z^2d_9^2k_9 + 2d_1\bar{k}_1(n_{1,1} - b_z n_{3,1}) + 2b_zd_{19}\bar{k}_{19}n_{3,19} - 2b_zd_2\bar{k}_{22}n_{3,2} + 2b_zd_{20}\bar{k}_{20}n_{3,20} + 2b_zd_{21}\bar{k}_{21}n_{3,21} + 2b_zd_{22}\bar{k}_{22}n_{3,22} + 2b_zd_{23}\bar{k}_{23}n_{3,23} + 2b_zd_2k_2a_{18}a_{13}a_{13} + 2b_zd_2\bar{k}_{22}n_{3,22} + 2b_zd_2k_6\bar{k}_{6}n_{3,6} - 2b_zd_7\bar{k}_{7}n_{3,7} - 2b_zd_8\bar{k}_{8}n_{3,8} - 2b_zd_9\bar{k}_{9}n_{3,9} - d_{10}^2k_{10} + 2d_{10}\bar{k}_{10}n_{1,10} - d_{12}^2k_{12} - 2d_{12}\bar{k}_{12}n_{1,12} - d_{13}^2k_{13} + 2d_{13}\bar{k}_{13}n_{1,13} - d_{15}^2k_{15} - 2d_{15}\bar{k}_{15}n_{1,15} - d_{16}^2k_{16} + 2d_{16}\bar{k}_{16}n_{1,16} - d_{18}^2k_{18} - 2d_{18}\bar{k}_{18}n_{1,18} - d_{19}^2k_{19} + 2d_{19}\bar{k}_{19}n_{1,19} - d_{21}^2k_{21} - 2d_{21}\bar{k}_{21}n_{1,21} - d_{22}^2k_{22} + 2d_{22}\bar{k}_{22}n_{1,22} - d_{24}^2k_{24} - 2d_{24}\bar{k}_{24}n_{1,24} - d_{25}^2k_{25} + 2d_{25}\bar{k}_{25}n_{1,25} - d_{27}^2k_{27} - 2d_{27}\bar{k}_{27}n_{1,27} - d_3^2k_3 - 2d_3\bar{k}_3n_{1,3} - d_4^2k_4 + 2d_4\bar{k}_4n_{1,4} - d_6^2k_6 - 2d_6\bar{k}_6n_{1,6} - d_7^2k_7 + 2d_7\bar{k}_7n_{1,7} - d_9^2k_9 - 2d_9\bar{k}_9n_{1,9})$ 

# Appendix D. The explicit expression for the term $\bar{f}_{14}$ in Eq. (25) in the case of nonzero source $f \neq 0$ in the Poisson equation

The expression for  $\bar{f}_{14}$  including the first two orders with respect to h is presented below. The expression for  $\bar{f}_{14}$  up to the eight order with respect to h is given in the attached file 'RHS-Pois.pdf'

$$\begin{split} & \bar{f}_{14} = \frac{\mathbf{h}_{2}^{\prime}}{2}(\mathbf{k}_{1}d_{1}^{2} - 2\bar{k}_{1}n_{1,1}d_{1} + d_{10}^{2}k_{10} + d_{12}^{2}k_{12} + d_{13}^{2}k_{13} + d_{15}^{2}k_{15} + d_{16}^{2}k_{16} + d_{18}^{2}k_{18} + d_{19}^{2}k_{19} + d_{21}^{2}k_{21} + d_{22}^{2}k_{22} + d_{24}^{2}k_{24} + d_{25}^{2}k_{25} + d_{27}^{2}k_{27} + d_{3}^{2}k_{3} + d_{4}^{2}k_{4} + d_{6}^{2}k_{6} + d_{7}^{2}k_{7} + d_{9}^{2}k_{9} - 2d_{10}\bar{k}_{10}n_{1,10} + 2d_{12}\bar{k}_{12}n_{1,12} - 2d_{13}\bar{k}_{13}n_{1,13} + 2d_{15}\bar{k}_{15}n_{1,15} - 2d_{16}\bar{k}_{16}n_{1,16} + 2d_{18}\bar{k}_{18}n_{1,18} - 2d_{19}k_{19}n_{1,19} + 2d_{21}\bar{k}_{21}n_{1,21} - 2d_{22}\bar{k}_{22}n_{1,22} + 2d_{24}\bar{k}_{24}n_{1,24} - 2d_{25}\bar{k}_{25}n_{1,25} + 2d_{27}\bar{k}_{27}n_{1,27} + 2d_{3}\bar{k}_{3}n_{1,3} - 2d_{4}\bar{k}_{4}n_{1,4} + 2d_{6}\bar{k}_{6}n_{1,6} - 2d_{7}\bar{k}_{7}n_{1,7} + 2d_{9}\bar{k}_{9}n_{1,9})f_{14} \\ &+ \frac{\mathbf{h}_{3}^{2}}{6}(3(\bar{k}_{1}n_{3,1}d_{1}^{2} + b_{z}(-k_{1}d_{1}^{3} + 2\bar{k}_{1}n_{1,1}d_{1}^{2} + d_{19}^{3}k_{19} + d_{21}^{3}k_{21} + d_{22}^{3}k_{22} + d_{24}^{3}k_{24} + d_{25}^{3}k_{25} + d_{27}^{3}k_{27} - d_{3}^{3}k_{3} - d_{4}^{3}k_{4} - d_{6}^{3}k_{6} - d_{7}^{3}k_{7} - d_{9}^{3}k_{9} - 2d_{19}^{2}\bar{k}_{19}n_{1,19} + 2d_{21}^{2}\bar{k}_{21}n_{1,21} - 2d_{22}^{2}\bar{k}_{22}n_{1,22} + 2d_{24}^{2}\bar{k}_{24}n_{1,24} - 2d_{25}^{2}\bar{k}_{25}n_{1,25} + 2d_{27}^{2}\bar{k}_{27}n_{1,27} - 2d_{3}^{2}\bar{k}_{3}n_{1,3} + 2d_{4}^{2}\bar{k}_{4}n_{1,4} + 2d_{25}^{2}\bar{k}_{25}n_{1,25} + 2d_{27}^{2}\bar{k}_{27}n_{1,27} - 2d_{3}^{2}\bar{k}_{3}n_{1,3} + 2d_{4}^{2}\bar{k}_{4}n_{1,4} + 2d_{4}^{2}\bar{k}_{4}n_$$

# Appendix E. Supplementary data

Supplementary material related to this article can be found online at https://doi.org/10.1016/j.cma.2020.112985.

#### References

- [1] H. Ahmadian, M. Friswell, J. Mottershead, Minimization of the discretization error in mass and stiffness formulations by an inverse method, Internat. J. Numer. Methods Engrg. 41 (2) (1998) 371–387.
- [2] M.N. Guddati, B. Yue, Modified integration rules for reducing dispersion error in finite element method, Comput. Methods Appl. Mech. Engrg. 193 (2004) 275–287.
- [3] V. Gyrya, K. Lipnikov, M-adaptation method for acoustic wave equation on square meshes, J. Comput. Acoust. 20 (2012) 1250022.
- [4] K.J. Marfurt, Accuracy of finite difference and finite element modeling of the scalar and elastic wave equation, Geophysics 49 (1984) 533–549.
- [5] R. Mullen, T. Belytschko, Dispersion analysis of finite element semidiscretizations of the two-dimensional wave equation, Internat. J. Numer. Methods Engrg. 18 (1982) 11–29.
- [6] B. Yue, M.N. Guddati, Dispersion-reducing finite elements for transient acoustics, J. Acoust. Soc. Am. 118 (4) (2005) 2132–2141.
- [7] Z.C. He, A.G. Cheng, G.Y. Zhang, Z.H. Zhong, G.R. Liu, Dispersion error reduction for acoustic problems using the edge-based smoothed finite element method (ES-FEM), Internat. J. Numer. Methods Engrg. 86 (11) (2011) 1322–1338.
- [8] A.V. Idesman, D. Pham, Accurate finite element modeling of acoustic waves, Comput. Phys. Comm. 185 (2014) 2034–2045.
- [9] M. Ainsworth, H.A. Wajid, Optimally blended spectral-finite element scheme for wave propagation and nonstandard reduced integration, SIAM J. Numer. Anal. 48 (1) (2010) 346–371.
- [10] D. Wang, W. Liu, H. Zhang, Novel higher order mass matrices for isogeometric structural vibration analysis, Comput. Methods Appl. Mech. Engrg. 260 (2013) 92–108.
- [11] D. Wang, W. Liu, H. Zhang, Superconvergent isogeometric free vibration analysis of Euler-Bernoulli beams and Kirchhoff plates with new higher order mass matrices, Comput. Methods Appl. Mech. Engrg. 286 (2015) 230–267.
- [12] V. Puzyrev, Q. Deng, V. Calo, Dispersion-optimized quadrature rules for isogeometric analysis: Modified inner products, their dispersion properties, and optimally blended schemes, Comput. Methods Appl. Mech. Engrg. 320 (2017) 421–443.
- [13] D. Wang, Q. Liang, J. Wu, A quadrature-based superconvergent isogeometric frequency analysis with macro-integration cells and quadratic splines, Comput. Methods Appl. Mech. Engrg. 320 (2017) 712–744.
- [14] A. Idesman, B. Dey, The use of the local truncation error for the increase in accuracy of the linear finite elements for heat transfer problems, Comput. Methods Appl. Mech. Engrg. 319 (2017) 52–82.
- [15] A. Idesman, B. Dey, New 25-point stencils with optimal accuracy for 2-D heat transfer problems. Comparison with the quadratic isogeometric elements, J. Comput. Phys. (2019) 1–41, submitted for publication.
- [16] A. Idesman, The use of the local truncation error to improve arbitrary-order finite elements for the linear wave and heat equations, Comput. Methods Appl. Mech. Engrg. 334 (2018) 268–312.
- [17] P. Vos, R. van Loon, S. Sherwin, A comparison of fictitious domain methods appropriate for spectral/hp element discretisations, Comput. Methods Appl. Mech. Engrg. 197 (25–28) (2008) 2275–2289.
- [18] E. Burman, P. Hansbo, Fictitious domain finite element methods using cut elements: I. A stabilized Lagrange multiplier method, Comput. Methods Appl. Mech. Engrg. 199 (41–44) (2010) 2680–2686.
- [19] E. Rank, S. Kollmannsberger, C. Sorger, A. Duster, Shell finite cell method: A high order fictitious domain approach for thin-walled structures, Comput. Methods Appl. Mech. Engrg. 200 (45–46) (2011) 3200–3209.
- [20] E. Rank, M. Ruess, S. Kollmannsberger, D. Schillinger, A. Duster, Geometric modeling, isogeometric analysis and the finite cell method, Comput. Methods Appl. Mech. Engrg. 249–252 (2012) 104–115.
- [21] S. May, M. Berger, An explicit implicit scheme for cut cells in embedded boundary meshes, J. Sci. Comput. 71 (3) (2017) 919–943.
- [22] A. Main, G. Scovazzi, The shifted boundary method for embedded domain computations. Part I: Poisson and Stokes problems, J. Comput. Phys. (2017).
- [23] T. Song, A. Main, G. Scovazzi, M. Ricchiuto, The shifted boundary method for hyperbolic systems: Embedded domain computations of linear waves and shallow water flows, J. Comput. Phys. 369 (2018) 45–79.
- [24] H.-O. Kreisst, N.A. Petersson, An embedded boundary method for the wave equation with discontinuous coefficients, SIAM J. Sci. Comput. 28 (6) (2006) 2054–2074.
- [25] H.-O. Kreiss, N.A. Petersson, A second order accurate embedded boundary method for the wave equation with Dirichlet data, SIAM J. Sci. Comput. 27 (4) (2006) 1141–1167.
- [26] H.-O. Kreiss, N.A. Petersson, J. Ystrom, Difference approximations of the Neumann problem for the second order wave equation, SIAM J. Numer. Anal. 42 (3) (2004) 1292–1323.
- [27] P. McCorquodale, P. Colella, H. Johansen, A cartesian grid embedded boundary method for the heat equation on irregular domains, J. Comput. Phys. 173 (2) (2001) 620–635.
- [28] H. Johansen, P. Colella, A Cartesian grid embedded boundary method for Poisson's equation on irregular domains, J. Comput. Phys. 147 (1) (1998) 60–85.
- [29] A. Idesman, A new numerical approach to the solution of partial differential equations with optimal accuracy on irregular domains and embedded Cartesian meshes. Part 1: the derivations for the wave, heat and Laplace equations in the 1-D and 2-D cases, Appl. Math. Model. (2019) 1–31, submitted for publication.
- [30] B. Dey, A. Idesman, A new numerical approach to the solution of partial differential equations with optimal accuracy on irregular domains and Cartesian meshes. Part 2: numerical simulation and comparison with FEM, Appl. Math. Model. (2019) 1 35, submitted for publication.
- [31] A. Idesman, B. Dey, A new 3-D numerical approach to the solution of PDEs with optimal accuracy on irregular domains and Cartesian meshes, Comput. Methods Appl. Mech. Engrg. 354 (2019) 568–592.